Structural and functional controls of artificial carbon materials based on domain structure model

金, 斗元

出版情報：九州大学, 2016, 博士（工学）, 課程博士
バージョン：
権利関係：

ドメイン構造モデルに基づく人造炭素材料の

構造および機能制御

Structural and functional controls of artificial carbon materials based on domain structure model

2017 年 1 月

九州大学

総合理工学府

量子プロセス理工学専攻

金　斗元

Doo-Won Kim

ドメイン構造モデルに基づく人造炭素材料の構造および機能制御

Structural and functional controls of artificial carbon materials based on domain structure model

指導教官： 宮脇　仁

2017 年 1 月

九州大学

総合理工学府大学院

量子プロセス理工学専攻

金　斗元

Doo-Won Kim

論文調査委員会

主査 九州大学 准教授　宮脇　仁

副査 九州大学 教授　　尹　聖昊

副査 九州大学 教授　　永長 久寛

Abstract

In modern world, carbon materials are used as one of the most important materials in various fields as electrode materials, adsorbents, composite materials for building materials and car body, and so on. By adequate treatments for raw materials (e.g. coal, petroleum, biomass, and natural gas) and/or precursors (e.g. pitch, coke, and polymer), diverse carbon materials having different properties, such as high tensile strength and high modulus carbon fibers, high specific surface area porous carbons, and high electrical and thermal conductive carbons. Although it is well-known that a configuration of hexagonal carbon layers in carbon materials governs the functional characteristics, more accurate and systematic understandings of the structure of carbon materials are indispensable for the further improvements of the performance. As a new conceptual model for carbon material structure, hierarchical domain structural model has been recently proposed. In this structural model, intermediate structural units connecting from molecular level to bulk (visible order) are newly introduced, which are graphene clusters (i.e. a stacked unit of hexagonal carbon layers), microdomains (i.e. an assembly of graphene clusters), and domains (i.e. an assembly of microdomains). The lower dimensional structure is considered to influence on the higher level, and eventually, on the macroscopic functional properties of carbon materials. Regardless of a finding of a presence of microdomains and domains for some of carbon materials, however, relationships between structures of microdomains/domains and macroscopic properties of carbon materials have not been clarified yet.

The objective of this study is to reveal an importance of the structural control of microdomains and domains to give high performance and high functionality to carbon materials by detailed analyses based on the hierarchical domain structural model.

In this thesis, the following research items regarding the structure analysis and function control of carbon materials were studied based on the hierarchical domain structure model; (1) confirmation of microdomain and domain structures of various carbon materials, (2) structure analysis of pore

development (activation) mechanism by different methods for activated carbons, (3) control of graphitization properties by partial destruction of structure of microdomains, and (4) improvement of electric conductivity as one of macroscopic properties by controlling of domain structure.

Contents of this thesis are summarized as follows;

In Chapter 1, brief introduction of structure in carbon materials, changes of structure and property of carbon materials depending on heat-treatment temperature, carbon structure models, and scope and objective of this thesis were described.

In Chapter 2, domain structures in various carbon materials were observed using the scanning tunneling microscopy (STM), and revealed that microdomain are basic structural unit for all artificial carbon materials. In addition, the difference of the size and shape of domains depending on the precursors and preparation method was confirmed.

In Chapter 3, based on the microdomain structural model, the activation mechanism which is an important at manufacturing process of activated carbon (AC) was elucidated from a structural point of view. Observation of the shape and size of the AC particles and microdomains prepared by physical activation (steam activation) and chemical activation (potassium hydroxide (KOH) activation) was used the scanning electron microscope (SEM) and STM. It revealed that AC preparation via KOH activation (chemical activation) did not induce noticeable changes in the particle or microdomain sizes, despite the remarkable development of pores. On the other hand, AC produced *via* steam activation (physical activation) showed remarkable reductions in both particle and microdomain sizes, depending on the activation temperature. Considering the differences in activation yield and degree of developed porosity between chemical and physical activations, it was concluded that, in the case of KOH activation, pore development homogeneously progressed overall for all microdomains consisting of carbon particles without apparent morphological change; however, steam activation caused inhomogeneous gasification from the outer surface of the carbon particles

and microdomains. For this reason, KOH-ACs showed higher yield and superior pore development. The proposed structural mechanism model for pore development with physical and chemical activations is expected to serve as a guideline for developing ACs with highly controlled pore structures.

In Chapter 4, highly graphitizable carbon was successfully prepared from typical non-graphitizable carbon (NGC) through a structural modification of the domain, one of the basic structural units of synthetic carbon materials, by high-temperature sodium hydroxide (NaOH) treatment. Analysis of the conversion mechanism, from non-graphitizable to graphitizable, using the nanostructure, as assessed with X-ray diffraction (XRD) and Raman spectroscopy; the meso-structure, as assessed with STM; and the macrostructure, as assessed with SEM, based on a novel hierarchical domain structure model, revealed that NaOH effectively destroyed microdomain boundaries, which enabled rearranging and merging of spherical microdomains to form a larger domain. The microdomains of NGCs showed distinct boundaries and independent structures that hindered or limited the degree of graphitization at the mesoscopic level. However, this limiting structure was changed by destroying the microdomain boundaries, thereby initiating rearrangement. The rearranged structure was similar to that of typical graphitizable carbon (GC), such as needle coke and meso-phase carbon fibers, which are arranged in one direction with an elongated shape. The present finding suggests that changing the domain structure allows control of the properties of carbon materials.

In Chapter 5, highly graphitized carbon with high electrical conductivity was successfully prepared from NGC *via* breaking-down and merging of boundaries of microdomains through the KOH treatment and subsequent graphitization. After the graphitization at 2800℃, the KOH-treated sample showed modified domains having merged boundaries between the microdomains which could be observed in GC. Such a domain-modified carbon showed less than half electrical resistivity of graphitized NGC, indicating that macroscopic properties, such as electrical conductivity, of

carbon materials can be improved *via* the modification of nanometer-scale microdomain and domain structures. From this results, it was concluded that control of the nanometer-scale structure of microdomains and domains is one of the key issues to control the macroscopic properties of the carbon material.

In Chapter 6, the novel findings obtained in this study were summarized as conclusion.

Contents

Chapter 1

General introduction

Carbon materials are one of the most important materials in many fields such as electrode materials, adsorbents, building materials and car body composites, etc. For improvement of properties, the understanding of the basic structure of carbon materials is required. In this chapter, the fundamental unit of hexagonal carbon layer in carbon materials are introduced. Furthermore, various carbon materials depending on heat-treatment temperature, and their properties which analyzed by diverse methods are also introduced. Finally, the conventional carbon structural models which help the understanding of carbon material structures and properties are presented.

1.1. Structure in carbon materials

The carbon materials are composed fundamental unit of hexagonal carbon layer. Properties of carbon materials is significantly changed depending on the stacking state of hexagonal carbon layer. Fig. 1-1 shows crystal structures for hexagonal and rhombohedral graphite. Hexagonal graphite composed *ABAB* stacking that means *A* and *B* as first layer and second layer, respectively [1,2]. On the other hand, rhombohedral graphite stacked at *ABCABC*, regularity[3,4]. In Fig. 1-2, hexagonal carbon layer and staking of graphitic / turbostratic structure are illustrated. Graphitic structure is *AB* stacking which are regularity staked to first layer (*A*) and second layer (*B*). On the other hand, turbostratic structure is *ABC* stacking of hexagonal graphite and rhombohedral graphite [5]. Turbostratic structure displace two kinds of state, displacive and rotational. Furthermore, the graphitizable carbon is composed parallel oriented staking of graphitic structure [6,7]. On the other hand, non-graphitizable carbon is

composed of randomly staking of rhombohedral structure. In order to study the structure of carbon materials, X-ray diffraction (XRD) is useful method [8-11]. In the XRD, graphitizable carbon have to be classified into three groups, the line with 00*l*, *hk*0 and *hkl* indices. The 00*l* indices defined basal planes (hexagonal carbon layers), *hk*0 indices are crystal planes perpendicular to the basal planes and *hkl* indices come from planes inclined relative to the basal plane. From this graphitic stacking of layer, graphitizable carbon is three-dimensional structure. By contrast, non-graphitizable carbon with turbostratic structure showed pattern of broad *00l* lines, unsymmetrical *hk* lines, and no *hkl* lines due to the small number of stacked layers and random stacking of layers. The planes perpendicular to layer planes are missing the *l* index, that is two dimensional structure [12-14]. A wide range of carbon structures depend primarily on the starting materials (precursors) and the heat-treatment temperature [15]. In table 1-1, classification of non-graphitizable carbon and graphitizable carbon in artificial carbon materials is described.

Table 1-2 tabulates various analytical methods of raw materials and carbon materials. The component (basic unit) analysis of carbon materials includes elemental analysis and X-ray fluorescence (XRF) analysis. Component analyses are important in carbon materials due to inference of basic molecular structure. The analyses of molecular structure include nuclear magnetic resonance (NMR), X-ray photoelectron spectroscopy (XPS), and infrared spectroscopy (IR). In carbon materials, bonding between molecules is a very important factor, because it affects on the physical / chemical properties. The molecular weight is analyzed by gas / liquid chromatography, time-of-flight mass spectrometry (TOF-MS), and etc. Molecular weight is important in petroleum / coal-based carbon materials. The XRD and Raman spectroscopy are the analyses (indirect) of the stacking structure of the molecules and graphitizability. Microscope is representative for direct structural analysis. Optical

microscope and scanning electron microscopy (SEM), transmission electron microscopy (TEM), and scanning tunneling microscopy (STM) can be used to observe surface structure and sizes of carbon materials.

Chemical / physical properties of the carbon materials which having various form of structures can be improved by the various analyzes.

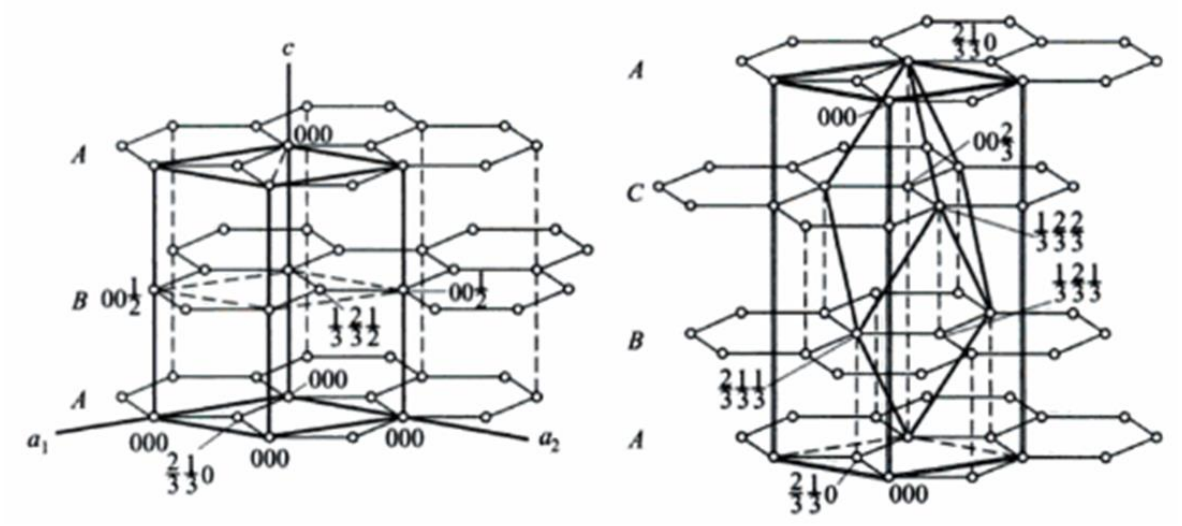

Fig.1-1. Crystal structures for two type of graphite.

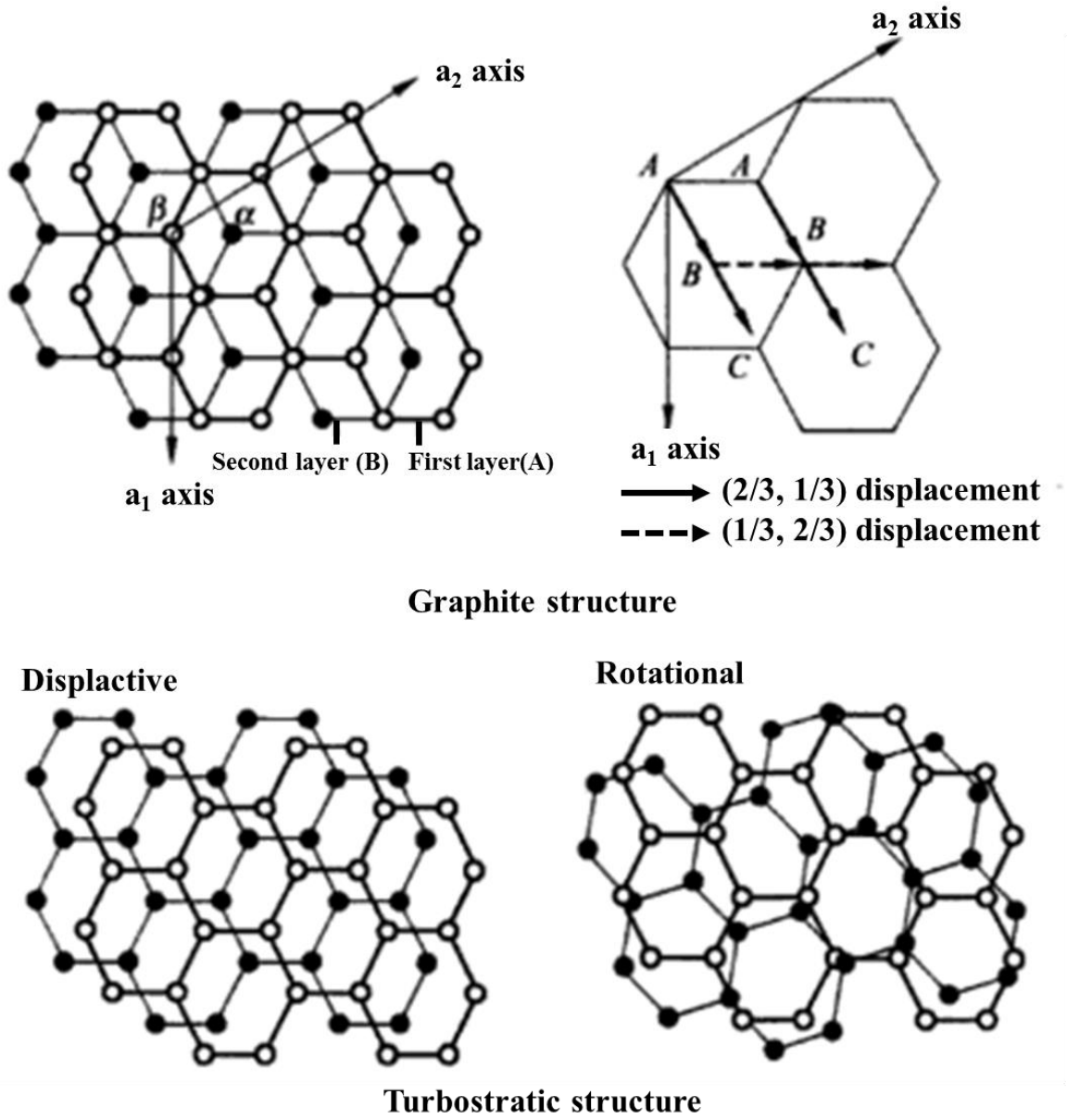

Fig. 1-2. Graphitic and turbostratic structures shown by stacking of two hexagonal carbon layers.

Table 1-1. Classification of non-graphitizable carbon and graphitizable carbon in artificial carbon materials.

	Non-graphitizable carbon	Graphitizable carbon
Precursor	Polymer, etc.	Isotropic & mesophase pitch, etc.
Material	PAN-based carbon fiber, isotropic coke, etc.	Mesophase-based carbon fiber, needle coke, etc.
Feature	Low gas permeability, etc.	High electrical & thermal conductivity, etc.
Crystallinity	Random staking	Oriented staking
Degree of graphitization (Over 2400℃ heat-treatment)	Low	High

Table 1-2. Various analytical methods of raw materials and carbon materials.

Analysis type	Analytical methods
Component analysis	Elemental analysis, X-ray fluorescence (XRF)
Molecular binding analysis	Nuclear magnetic resonance (NMR), X-ray photoelectron spectroscopy (XPS), Infrared spectroscopy (IR).
Molecular weight analysis	Gas / liquid chromatography, Time-of-flight mass spectrometry (TOF-MS)
Structure analysis (Indirectly)	X-ray diffraction (XRD), Raman spectroscopy
Structure analysis (Directly)	Optical microscopy, Scanning electron microscopy (SEM), Transmission electron microscopy (TEM), Scanning tunneling microscopy (STM)

1.2. Changes of structure and property of carbon materials depending on heat-treatment temperature

Carbon materials are greatly affected by the heat-treatment temperature. Fig. 1-3 shows manufacturing condition of carbon materials, and changing of structure depending on the heat-treatment temperature [16,17]. In the phase of reaction, all of phase, vapor, solid, and liquid can be manufactured as various carbon materials by the heat treatment. Also, precursors exist such as coal, petroleum, polymer, and biomass, etc. In case of vapor, carbon materials prepared by the radical pyrolysis about 400 ~ 1200℃ [18]. The solid phase is changed as carbonaceous materials by the crosslinking below 600℃. After then, various carbon materials prepared that carbonaceous materials are heated at over 600℃ in the inert atmosphere for developing of carbon structure such as cluster (hexagonal carbon layer and its stacking). The liquid state is treated to aromatization and poly-condensation about 300 ~ 500℃, and it is changed carbon structure after coking [19-21]. And then, carbon materials prepared by the heat-treatment above 600℃. Some materials can be prepared to synthetic graphite with about 3000℃ heat-treatment [22].

In the application, the carbon materials which prepared by vapor phase are pyro-carbon above 600℃, fibrous carbons such as prepared chemical vapor deposition (CVD) at 600 ~ 1000℃ [23-27], artificial graphite which prepared high temperature (above 3000℃) under high pressure. From solid and liquid phase, activated carbons are prepared by the activation at the 600 ~ 1000℃ [28-30]. And glassy or hard carbons, and needle coke at the over 1000℃, carbon fiber with high tensile strength are prepared [31]. Above 2000℃, glassy carbon, carbon fiber with high modulus, carbon/carbon composite, and graphite electrode are manufactured. Highly oriented pyrolytic graphite (HOPG) which well-developed graphite

structure like nature graphite is prepared above 3000℃. Various carbon materials can be produced depending on the heat-treatment temperature.

Depending on the temperature, carbon structure is developed such as staking of hexagonal carbon layer (L_c(002)) and planar (L_a(110)), and porosity. Around 500℃, cluster nuclei are generated. L_a(110) size increases from 600℃ with increasing of temperature. L_c(002) is developed from about 1000℃. Representing a three-dimensional structure, L_a(112) is generated at the above 2400℃ which is significantly developed in graphitizable carbon materials. In case of porosity, carbon materials activated at 600 ~ 1000℃ with active agent such as steam, carbon hydroxide, potassium, zinc chloride, etc. Normally, micropore structure developed at 1000℃, but over the 1000℃, micropore is decreased [32].

Fig. 1-4 summarized about the properties of various carbon materials [15]. In the case of electrical conductivity, carbon intercalation compounds show higher electrical conductivity than natural graphite. HOPG and graphite whisker also exhibit fairly high electrical conductivity. The graphite (single crystal) showed higher tensile strength in carbon materials. The graphite whisker, and PAN-based carbon fiber which is widely used as a composite material for aerospace, exhibits a high tensile strength. Among the various carbon materials, carbon fibers which prepared different type manufacturing showed. As the specific surface area, industrial phenol-based activated carbon fibers have a high specific surface area up to 2500 m^2 g^{-1}. The specific surface area is controlled by the activation time, activation temperature, and activation agents. In addition, activation can be achieved by using various carbon materials.

Various types of carbon materials can be prepared according to the raw materials. Carbon materials are used wide field due to wide range chemical / physical properties. Therefore,

understanding of the structure of the carbon material is required, and improvement of properties according to application are essential.

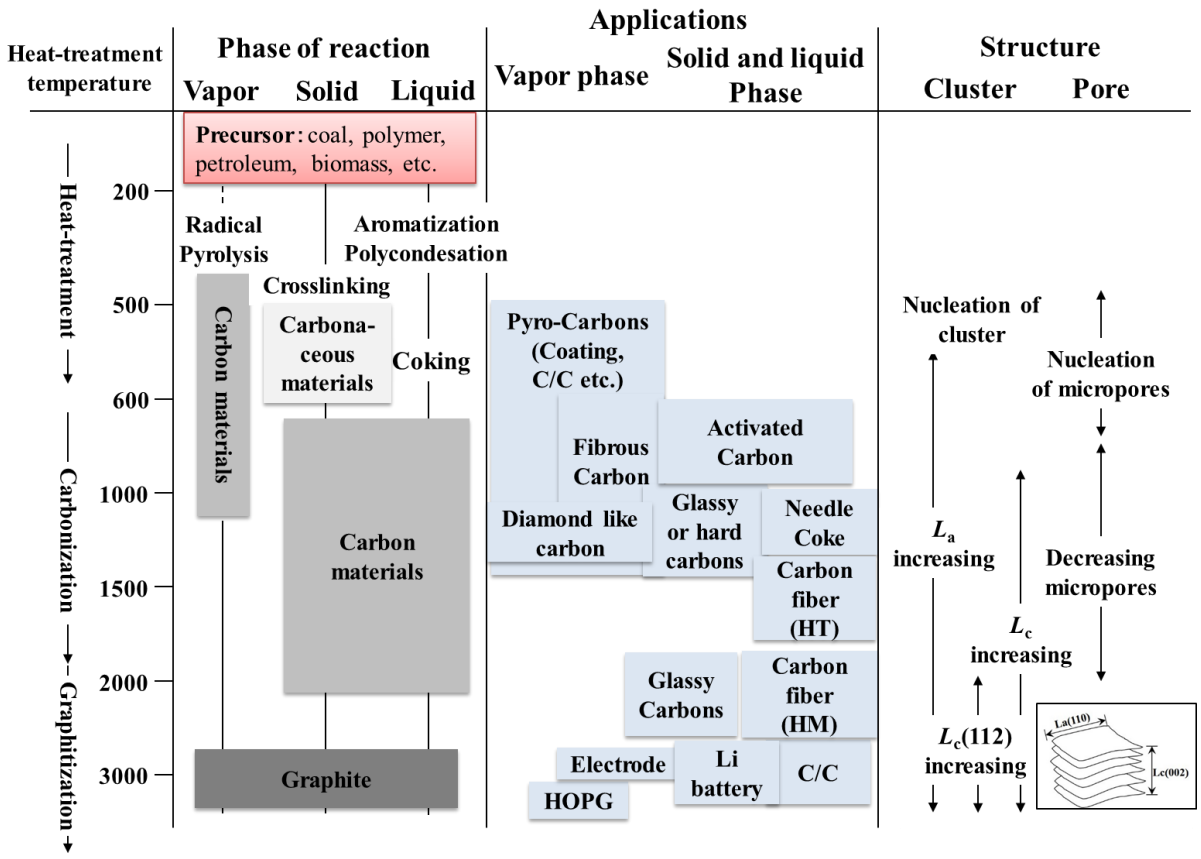

Fig. 1-3. Depending on the heat-treatment temperature, manufacturing condition of carbon materials, and changing of structure.

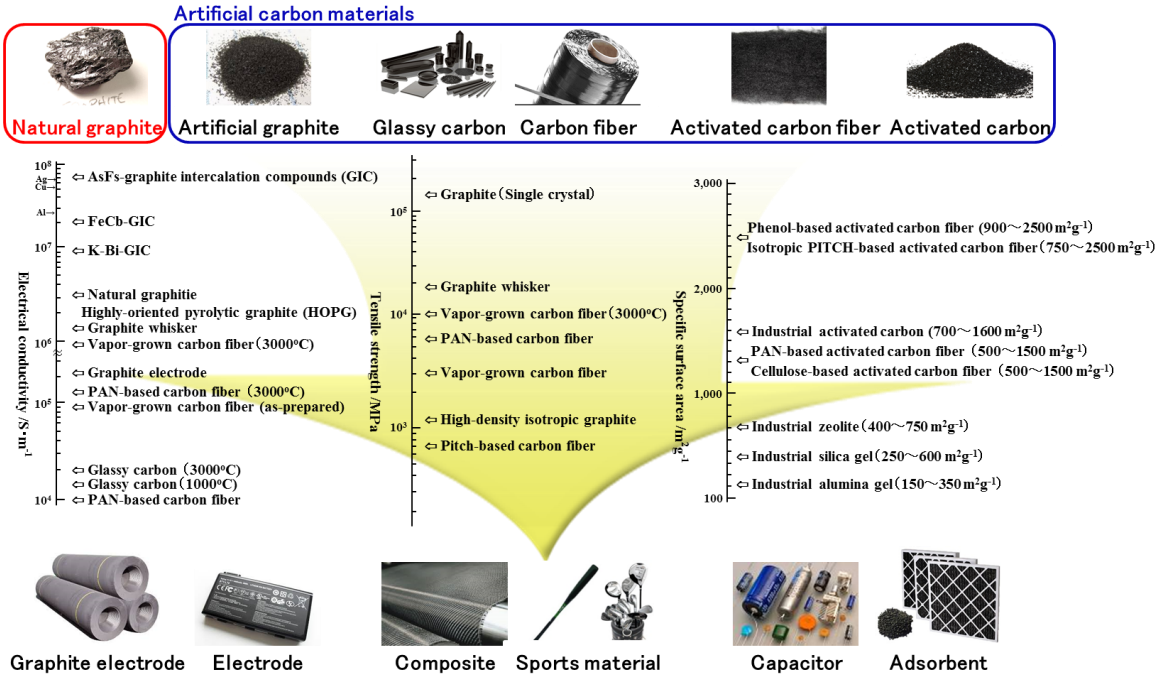

Fig. 1-4. Properties of various carbon materials, and these applications.

1.3. Carbon structure models

Studies on the structure of carbon materials have been progressed with various analysis methods. However, in the early days, analyses of given the indirect information has the main. Thus, for help of understand the carbon structures needed for a structural model. As the analysis method evolved, various structural models were proposed using the analyses of given direct / indirect information. Below, it is presented as the structural models of a representative carbon materials.

Franklin model

The basic structure of the carbon material is a hexagonal carbon layer. It is classified into graphitizable / non-graphitizable according to stacking state. In 1951, Franklin proposed the graphitizable and non-graphitizable carbon structure model two-dimensionally using the XRD in Fig 1-5 [33,34]. Graphitizable carbon shows the oriented molecular structure which are located in parallel regularly. On the other hand, molecular orientation non-graphitizable carbon is located randomly. In addition, it reported that non-graphitizable carbon is a strong system of cross-linking uniting the crystallites, whereas graphitizable carbon the cross-linking is much weaker, the structure is more compact. In non-graphitizable carbon, the growth of crystallite is very limited within the size of their randomly orientation. Therefore, non-graphitizable carbons convert to carbon materials with very low degree of graphitization, low apparent density even after heat treatment above 2400^{o}C. On the other hand, graphitizable carbon is relatively easy to grow in crystallinity because of their planar orientation after heat treatment above 2400^{o}C. Therefore, carbon materials with a high degree of graphitization and with a high density are obtained from graphitizable carbon.

Ribbon model

In 1971, Johnson et al, suggested Ribbon model about glassy carbon (non-graphitizable carbon) using the high resolution TEM in Fig. 1-6 [35]. Moreover, crystallite such as $L_c(002)$ and $L_a(10)$ considered from the XRD analysis results. In addition, this model assumes that the molecular orientation in the polymer precursor materials is retained to some extent after carbonization. Ribbon model entails the formation of micropores because of inefficient packing in an isotropic assembly of ribbons, resulting in a low density compared with single crystals of graphite. According to this model, the fibrils in the polymer become curved and twisted ribbons of graphite-like carbon.

Shell model

In 1984, Shiraishi M, suggested shell model that heat-treated glassy carbon was observed with TEM [36], in the same way as ribbon model. In Fig. 1-6, Shell model involves cage-like components enclosing closed pores and considered to be realistic. Hexagonal layers are locally oriented in a concentric cell-like structures with around 5 nm of diameter. Compared to the previous Franklin model and Ribbon model, the size was clearly presented. In addition, one of the feature in glassy carbon, the closed pore is clearly expressed.

Domain model

In 1996, our group suggested a 3-D structural model of mesophase pitch-based carbon fiber (MPCF) from combined analyses with scanning electron microscopy (SEM), scanning tunneling microscopy (STM) [37]. Fig. 1-7 is explained that the domain-based structural

analysis of carbon material into a hierarchical domain structural analysis [16]. Hierarchical domain structural analysis of carbon material can be explained as the serial formation of carbon structures from molecules (e.g., a hexagonal carbon layer), molecular assemblies (e.g., stacked units), microdomains (an assembly of stacked units), domains (an assembly of microdomains), and bulk (an assembly of domains). Based on this hierarchical domain structural analysis, analysis to the pore formation mechanism in activated carbon fibers [38]; an examination of the relationship between the physical properties and the structures of polyacrylonitrile (PAN) and pitch-based carbon fibers [39] was conducted. Consequently, hierarchical domain structural model can be explained the relationship between structure and physical properties, effectively.

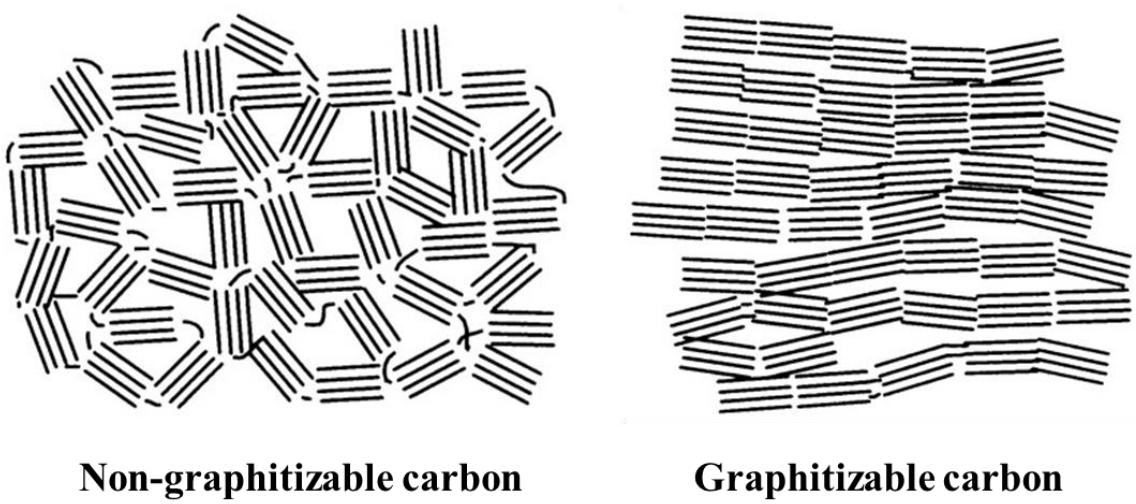

Fig. 1-5. Franklin model of non-graphitizable carbon and graphitizable carbon in two dimensional. ("Reprinted from Journal of Proceedings of the Royal Society of London A, 209 / 4015780891078, Franklin, RE., Crystallite Growth in Graphitizing and Non-Graphitizing Carbons, 196-218, 1951, with permission from The Royal Society.")

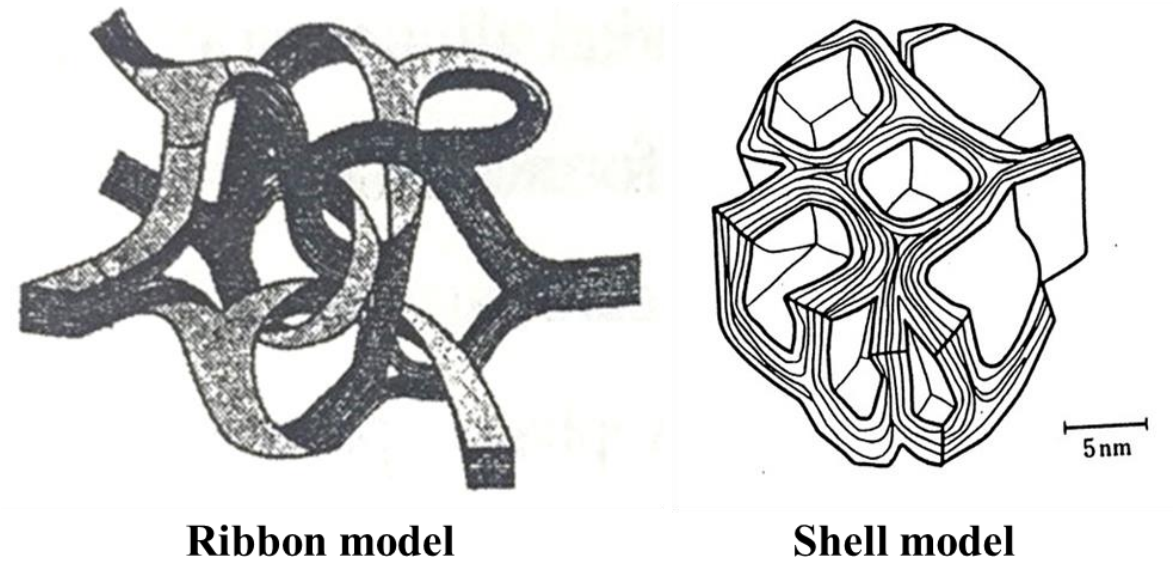

Fig. 1-6. Ribbon model and Shell model in three dimensional. ("Reprinted from Journal of Nature, 231 / 4015741016778, Jenkins GM., et. al., Structure of Glassy Carbon, 175-176, 1971, with permission from Nature Publishing Group and Copyright Clearance Center.")

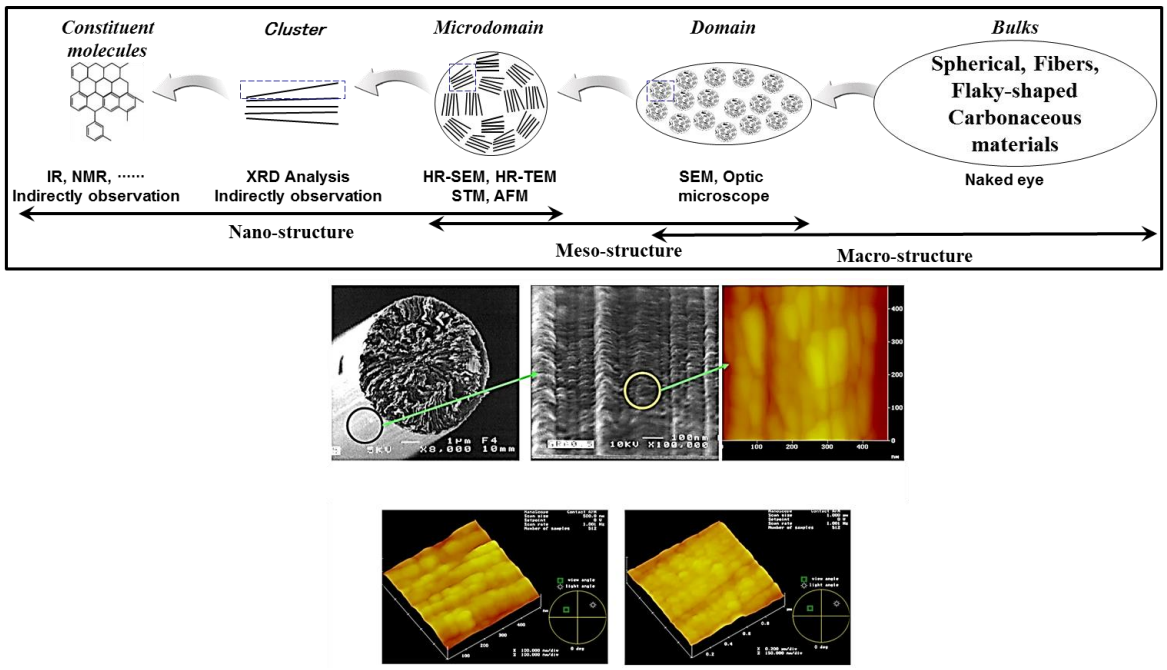

Fig. 1-7. Structural hierarchy of mesophase pitch based carbon fibers assembly of microdomains (pleats) and domains. ("Reprinted from Journal of Carbon, 34 / 4015770476407, Yoon, SH., et.al, Axial nano-scale microstructures in graphitized fibers inherited from liquid crystal mesophase pitch, 83-88, 1996, with permission from Elsevier.")

1.4 Scope and objectives of this thesis

Carbon materials are one of the most important materials in many fields such as electrode materials, adsorbents, building materials and car body composites, etc. However, as the industry develops, various carbon materials are required that improvement of properties, and control / modification of functions for more efficient application in wide range fields. In order to improve the properties, and control / modification of functions, understanding of the carbon structure is essential. To understand of the carbon structure, many studies have been reported using diverse analysis methods. In addition, many structural models have been proposed to help understanding of structure. However, most of the studies have focused on how micro-structure of carbon materials is, and elucidations about relationships between the macroscopic functions and structure are still limited. Therefore, a more hierarchical structural approach is required.

In this thesis, from hierarchical domain structure model, I challenged in structure analysis and function control of carbon materials. Especially, using the microdomain which is (1) observed the basic structural units of all artificial carbon materials, (2) structure analysis (activation mechanism) of carbon materials, and (3) control of properties (graphitization degree and electrical resistance) were performed.

Contents of this thesis are summarized as follows;

In Chapter 1, brief introduction of structure in carbon materials, changes of structure and property of carbon materials depending on heat-treatment temperature, carbon structure models, and scope and objective of this thesis were described.

In Chapter 2, domain structures in various carbon materials were observed using the scanning tunneling microscopy (STM), and revealed that microdomain are basic structural unit for all artificial carbon materials. In addition, the difference of the size and shape of domains depending on the precursors and preparation method was confirmed.

In Chapter 3, based on the microdomain structural model, the activation mechanism which is an important at manufacturing process of activated carbon (AC) was elucidated from a structural point of view. Observation of the shape and size of the AC particles and microdomains prepared by physical activation (steam activation) and chemical activation (potassium hydroxide (KOH) activation) was used the scanning electron microscope (SEM) and STM. It revealed that AC preparation via KOH activation (chemical activation) did not induce noticeable changes in the particle or microdomain sizes, despite the remarkable development of pores. On the other hand, AC produced *via* steam activation (physical activation) showed remarkable reductions in both particle and microdomain sizes, depending on the activation temperature. Considering the differences in activation yield and degree of developed porosity between chemical and physical activations, it was concluded that, in the case of KOH activation, pore development homogeneously progressed overall for all microdomains consisting of carbon particles without apparent morphological change; however, steam activation caused inhomogeneous gasification from the outer surface of the carbon particles and microdomains. For this reason, KOH-ACs showed higher yield and superior pore development. The proposed structural mechanism model for pore development with physical and chemical activations is expected to serve as a guideline for developing ACs with highly controlled pore structures.

In Chapter 4, highly graphitizable carbon was successfully prepared from typical non-graphitizable carbon (NGC) through a structural modification of the domain, one of the basic structural units of synthetic carbon materials, by high-temperature sodium hydroxide (NaOH) treatment. Analysis of the conversion mechanism, from non-graphitizable to graphitizable, using the nanostructure, as assessed with X-ray diffraction (XRD) and Raman spectroscopy; the meso-structure, as assessed with STM; and the macrostructure, as assessed with SEM, based on a novel hierarchical domain structure model, revealed that NaOH effectively destroyed microdomain boundaries, which enabled rearranging and merging of spherical microdomains to form a larger domain. The microdomains of NGCs showed distinct boundaries and independent structures that hindered or limited the degree of graphitization at the mesoscopic level. However, this limiting structure was changed by destroying the microdomain boundaries, thereby initiating rearrangement. The rearranged structure was similar to that of typical graphitizable carbon (GC), such as needle coke and meso-phase carbon fibers, which are arranged in one direction with an elongated shape. The present finding suggests that changing the domain structure allows control of the properties of carbon materials.

In Chapter 5, highly graphitized carbon with high electrical conductivity was successfully prepared from NGC *via* breaking-down and merging of boundaries of microdomains through the KOH treatment and subsequent graphitization. After the graphitization at 2800℃, the KOH-treated sample showed modified domains having merged boundaries between the microdomains which could be observed in GC. Such a domain-modified carbon showed less than half electrical resistivity of graphitized NGC, indicating that macroscopic properties, such as electrical conductivity, of carbon materials can be improved *via* the modification of

nanometer-scale microdomain and domain structures. From this results, it was concluded that control of the nanometer-scale structure of microdomains and domains is one of the key issues to control the macroscopic properties of the carbon material.

In Chapter 6, the novel findings obtained in this study were summarized as conclusion.

References

[1] Bernal, J. D. "The structure of graphite." *Proceedings of the Royal Society of London. Series A, Containing Papers of a Mathematical and Physical Character* **106** (1924): 749–773.

[2] Hassel, O., and Mark, H. Z. "Ü ber die Kristallstruktur des Graphits", *Zeitschrift für Physik* **25** (1924): 317–337.

[3] Lipson, H., and Stokes, A. R. "A new structure of carbon." *Nature* **149** (1942): 328–328.

[4] Lipson, H., and Stokes, A. R. "The structure of graphite." *Proceedings of the Royal Society of London A: Mathematical, Physical and Engineering Sciences*. The Royal Society, **181** (1942): 101–105.

[5] Nelson, J. B., and Riley, D. P. "The thermal expansion of graphite from 15 c. to 800 c.: Part I. Experimental." *Proceedings of the Physical Society* **57** (1945): 477.

[6] Warren, B. E. "X-Ray Diffraction Study of Carbon Black." *The Journal of Chemical Physics* **2** (1934): 551–555.

[7] Endo, M., et al. "Evidence for glide and rotation defects observed in well-ordered graphite fibers." *Journal of materials research* **10** (1995): 1461–1468.

[8] Zhao, Y. X., and Spain, I. L. "X-ray diffraction data for graphite to 20 GPa." *Physical Review B* **40** (1989): 993.

[9] Yagi, T., et al. "High-pressure in situ x-ray-diffraction study of the phase transformation from graphite to hexagonal diamond at room temperature." *Physical Review B* **46** (1992): 6031.

[10] Li, Z. Q., et al. "X-ray diffraction patterns of graphite and turbostratic carbon." *Carbon* **45** (2007): 1686–1695.

[11] Jeong, H. K., et al. "Evidence of graphitic AB stacking order of graphite oxides." *Journal of the American Chemical Society* **130** (2008): 1362–1366.

[12] Bacon, G. E. "Unit-cell dimensions of graphite." *Acta Crystallographica* **3** (1950): 137–139.

[13] Nakamizo, M., Honda, H., and Inagaki, M. "Raman spectra of ground natural graphite." *Carbon* **16** (1978): 281–283.

[14] Boehm, H. P., and Coughlin, R. W. "Enthalpy difference of hexagonal and rhombohedral graphite." *Carbon* **2** (1964): 1–6.

[15] Inagaki, M., and Kang, F. *Carbon Materials Science and Engineering: From Fundamentals to Applications*. Tsinghwa university Press, Beijing, 2006.

[16] Mochida, I., et al. "Progress and effectiveness of structural models of carbons." *Tanso (Japanese)* **215** (2004): 274–284.

[17] Oberlin, A. "Carbonization and graphitization." *Carbon* **22** (1984): 521–541.

[18] Bokros, J. C. "The structure of pyrolytic carbon deposited in a fluidized bed." *Carbon* **3** (1965): 17–29.

[19] Choudhary, V. R., et al. "H-gallosilicate (MFI) propane aromatization catalyst: Influence of Si/Ga ratio on acidity, activity and deactivation due to coking." *Journal of Catalysis* **158** (1996): 34–50.

[20] Lu, Y., et al. "A high coking-resistance catalyst for methane aromatization." *Chemical Communications* **20** (2001): 2048–2049.

[21] Choudhary, V. R., et al. "Characterization of coke on H-gallosilicate (MFI) propane aromatization catalyst.: Influence of coking conditions on nature and removal of coke." *Microporous and Mesoporous Materials* **21** (1998): 91–101.

[22] Dawson, I. M., and Follett, E. A. C. "An electron microscope study of synthetic graphite." *Proceedings of the Royal Society of London A: Mathematical, Physical and Engineering Sciences*. The Royal Society, **253** (1959).

[23] Thostenson, E. T., et al. "Carbon nanotube/carbon fiber hybrid multiscale composites." *Journal of Applied physics* **91** (2002): 6034–6037.

[24] Li, Y. L., Kinloch, I. A., and Windle, A. H. Windle. "Direct spinning of carbon nanotube fibers from chemical vapor deposition synthesis." *Science* **304** (2004): 276–278.

[25] Kim, T. G., et al. "Electrochemical capacitances of well-defined carbon surfaces." *Langmuir* **22** (2006): 9086–9088.

[26] Che, G., et al. "Chemical vapor deposition based synthesis of carbon nanotubes and nanofibers using a template method." *Chemistry of Materials* **10** (1998): 260–267.

[27] Ahmadpour, A., and Do, D. D. "The preparation of activated carbon from macadamia nutshell by chemical activation." *Carbon* **35** (1997): 1723–1732.

[28] Rodriguez-Reinoso, F., Molina-Sabio, M. and Gonzalez, M. T. "The use of steam and CO_2 as activating agents in the preparation of activated carbons." *Carbon* **33** (1995): 15–23.

[29] Hayashi, J., et al. "Preparation of activated carbon from lignin by chemical activation." *Carbon* **38** (2000): 1873–1878.

[30] Caturla, F., M. Molina-Sabio, and F. Rodriguez-Reinoso. "Preparation of activated carbon by chemical activation with ZnCl2." *Carbon* **29** (1991): 999–1007.

[31] Kim, B. J., et al. "Preparation of carbon fibers with excellent mechanical properties from isotropic pitches." *Carbon* **77** (2014): 747–755.

[32] Yoon, S. H., et al. "KOH activation of carbon nanofibers." *Carbon* **42** (2004): 1723–1729.

[33] Franklin, R. E. "The structure of graphitic carbons." *Acta crystallographica* **4** (1951): 253–261.

[34] Franklin, R. E. "Crystallite growth in graphitizing and non-graphitizing carbons." *Proceedings of the Royal Society of London A: Mathematical, Physical and Engineering Sciences*. The Royal Society, **209** (1951).

[35] Jenkins, G. M., and Kawamura, K. "Structure of glassy carbon." *Nature* **231** (1971): 175–176.

[36] Shiraishi, M. *Kaitei Tansozairyou Nyuumon (Japanese)*. (1984): 29–44.

[37] Yoon, S. H., et al. "Axial nano-scale microstructures in graphitized fibers inherited from liquid crystal mesophase pitch." *Carbon* **34** (1996): 83–88.

[38] Shiratori, N., et al. "Pore structure analysis of activated carbon fiber by microdomain-based model." *Langmuir* **25** (2009): 7631–7637.

[39] Li, W., et al. "Structural features of polyacrylonitrile-based carbon fibers." *Journal of materials science* **47** (2012): 919–928.

Chapter 2

Observation of domain structure in various carbon materials

2.1. Introduction

Our group proposed a hierarchical carbon structure model [1]. Hierarchical domain structural analysis of carbon material can be explained as the serial formation of carbon structures from molecules (e.g., a hexagonal carbon layer), molecular assemblies (e.g., stacked units), microdomains (an assembly of stacked units), domains (an assembly of microdomains), and bulk (an assembly of domains).

Based on the domain structure model, it is applied such a hierarchical domain structural analysis to the pore formation mechanism in activated carbon fibers [2]. In this previous study, it has been revealed that each activated carbon particle consists of numerous spherical microdomains, a basic structural unit, by scanning tunneling microscopy (STM) observations. Furthermore, unlike the conventional hierarchical pore structure model, in the microdomain structure model, micropores develop in each microdomain, and mesopores form between adjacent microdomains (i.e., in inter-microdomain space). In addition, an examination of the relationship between the physical properties and the structures of polyacrylonitrile (PAN) and pitch-based carbon fibers [3] is conducted using the domain structure. PAN-based carbon fiber showed that The size and shape of these particles strongly depended on the precursor composition, process condition as well as the heat-treated temperature.

From domain structure model, it can be explained that interpretation of carbon structure (mechanism) and relationship of domain structure and properties. However, it was considered that whether the microdomain structure existed as a basic structure unit in all the carbon

materials. For that reason, in this study, the microdomain structures of various carbon materials were observed using the STM. In addition, microdomains were classified according to the raw materials (precursors).

2.2. Experimental

2.2.1. Sample preparations

To obtain graphitized samples, needle and isotropic cokes (from a Japanese company) were further heat-treated at 2800℃ for 10 min under an Ar atmosphere, in a horizontal tubular-type graphitization furnace (Kurata Giken Co., Ltd., Japan).

A PAN-based carbon nano fiber were prepared *via* electro-spinning process. 8 wt. % homo polyacrylonitrile (PAN, Mw 150,000 g/mol, WAKO chemical Ltd.) was dissolved in N,N'-dimethylformamide. The electro-spinning condition was: tip to collector distance, 15 cm; applied voltage, 30 kV: dope feeding rate, 2 mL/h After electro-spinning, spun-fiber heat-treated at 270ºC for 1 h at a ramping rate of 1℃ min^{-1} with air condition (stabilization). After then, stabilized fiber heat-treated at 750ºC for 1 h at a ramping rate of 5℃ min^{-1} in N_2 flow (200 mL min^{-1}) (carbonization).

Thermo-set spherical phenol resin-based beads resin (BEAPS series, Asahi Yukizai Corporation, Japan) were treated at 600℃ for 1 h at a heating rate of 5℃ min^{-1} under a N_2 flow.

Cellulose-based activated carbon fiber was received at East China University.

2.2.2. Characterization

To observe the domains, STM observation of the prepared various carbon materials was carried out after heat treatment at 600℃ under a H_2:Ar (1:4) atmosphere, to remove noise originating from heteroatoms. The STM images were acquired in constant current mode (current range: 0.1–1.0 nA; bias voltage: 0.1–2.0 V; scan frequency: 1–2 Hz) using an

Agilent Technologies 5500 Scanning Probe Microscope (Toyo Corporation, Japan). The particle size was estimated using SEM (JSM-6700F, JEOL, Japan).

2.3. Results and discussion

In Fig. 2-1, the domain structure images of various carbon materials were classified according to the precursors. In precursor of biomass, domain structures of cellulose-based activated carbon fiber (ACF) and mangrove-based carbon were observed. Cellulose-based ACF composed small size independent microdomain. The mangrove-based carbon [4] showed large independent microdomain structure compared with another microdomain structure.

In coal and petroleum based carbon materials, such as pitch-based ACF [2], isotropic coke, and needle coke were observed. Pitch-based ACF showed independent microdomain of average diameter of 5.75 nm size with spherical shape. In case of coke samples, isotropic coke and needle coke showed very different microdomain structure in spite of the precursor of coke. Isotropic coke presented the independent of spherical microdomain structure. On the other hand, needle coke presented elongated domain structure by the merged microdomain structure.

In the polymer based carbon materials, PAN-based ACF [2], PAN-based carbon fiber (CF) [3], PAN-based carbon nano fiber (CNF) *via* prepared electro-spinning, and phenol-resin based carbon were observed. PAN-based ACF showed a very different type of microdomain structure compared with cellulose- and pitch-based ACF. Although the material is used for similar fields, the microdomain structure is very different. PAN-based CF showed independent microdomain structure arranged in one direction, which is different of needle coke (merged microdomain). In case of PAN-based CNF prepared electro-spinning, microdomain structure showed very small and strange shape compared with another microdomain. This is presumably due to a special spinning method of electro-spinning. Even though the same precursor is used such as PAN-based precursor, PAN-based CF / ACF and

PAN-based CNF presented that according to the manufacturing method, the microdomain structures are a notable difference. Microdomain structure of phenol-resin based carbon was observed as spherical shape and independent microdomain like isotropic coke.

Herringbone CNF [5], carbon nano rods, fullerene, and glassy carbon were observed as various type carbon materials. In case of various type carbon materials, their showed different size and shape of microdomains.

From Fig. 2-1, all artificial carbon materials revealed that microdomain is basic structural unit. In addition, the difference of the size and shape of microdomains depending on the precursors and preparation method was confirmed.

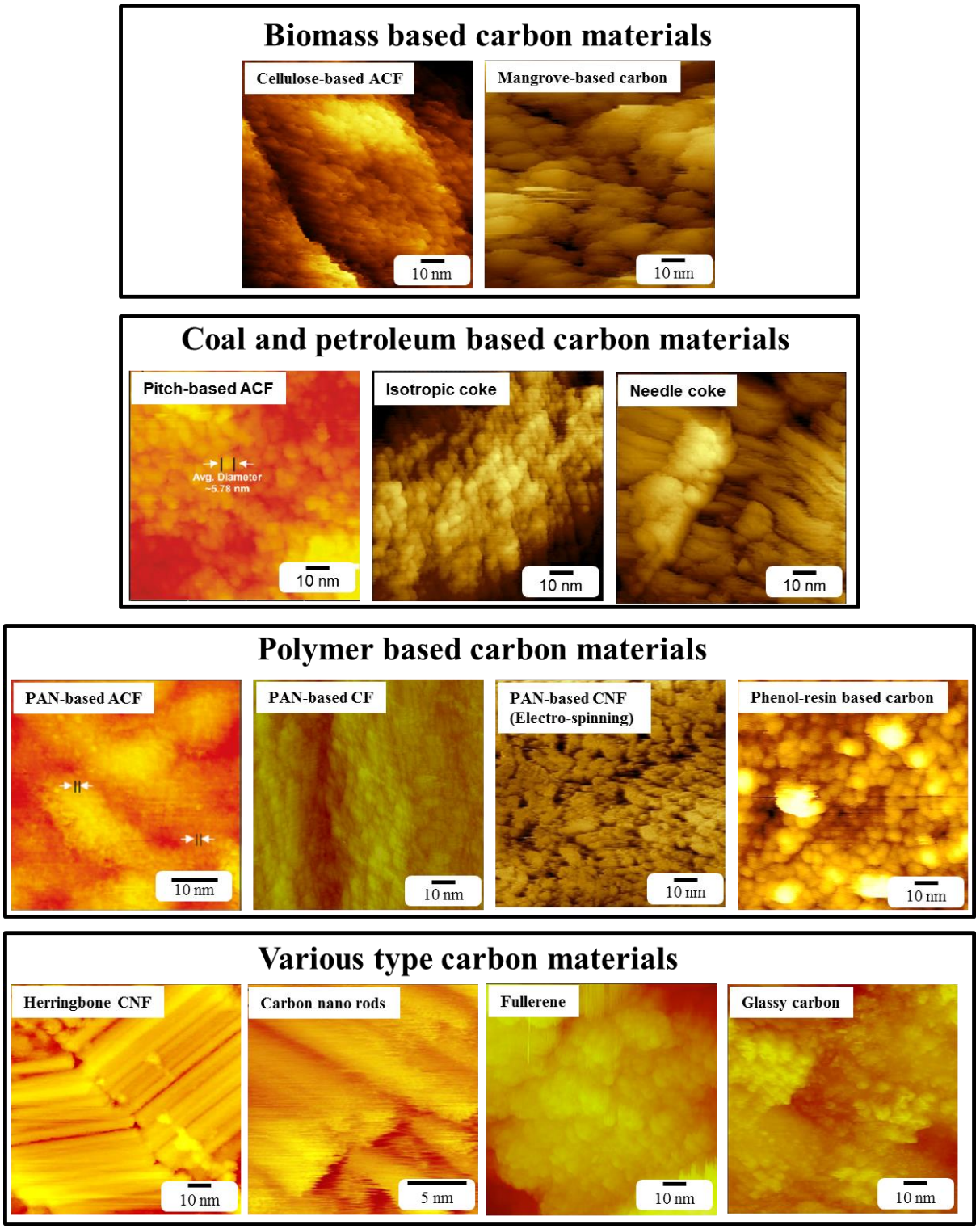

Fig. 2-1. Microdomain structures of various carbon materials. (To express of information about rights and permissions of some images in the acknowledgements)

2.4. Conclusions

Domain structures in various carbon materials were observed using the scanning tunneling microscopy (STM), and revealed that microdomain are basic structural unit for all artificial carbon materials. In addition, the difference of the size and shape of microdomains depending on the precursors and preparation method was confirmed. Therefore, considering of the previous domain studies, the domain structure will affect the structural and functional controls of the carbon materials.

Acknowledgements

I appreciated that permission of image reuse in a dissertation / thesis. Below, information about rights and permissions are expressed.

Reprinted from Journal of Langmuir, 25 / 10.1021/la9000347, Shiratori, N., et. al., Pore Structure Analysis of Activated Carbon Fiber by Microdomain-Based Model, 7631-7637, 2009, with permission from American Chemical Society.

Reprinted from Journal of Materials Science, 47 / 4015760836444, Li, W., et. al., Structural features of polyacrylonitrile-based carbon fibers, 919-928, 2012, with permission from Springer.

Reprinted from Journal of Carbon, 43 / 4015761342223, Yoon, SH., et. al., A conceptual model for the structure of catalytically grown carbon nano-fibers, 1828-1838, 2005, with permission from Elsevier.

References

[1] Mochida, I., et al. "Progress and effectiveness of structural models of carbons." *Tanso (Japnanese)* **215** (2004): 274–284.

[2] Shiratori, N., et al. "Pore structure analysis of activated carbon fiber by microdomain-based model." *Langmuir* **25** (2009): 7631–7637.

[3] Li, W., et al. "Structural features of polyacrylonitrile-based carbon fibers." *Journal of Materials Science* **47** (2012): 919–928.

[4] Han, Y. J., et al. "Effect of heat pre-treatment conditions on the electrochemical properties of mangrove wood-derived hard carbon as an effective anode material for lithium-ion batteries." *Electrochimica Acta* **213** (2016): 432–438.

[5] Yoon, S. H., et al. "A conceptual model for the structure of catalytically grown carbon nano-fibers." *Carbon* **43** (2005): 1828–1838.

Chapter 3

Structural elucidation of physical and chemical activation mechanisms based on the microdomain structure model

3.1. Introduction

Activated carbons (ACs) are used as adsorbents in water and air purification [1,2] and gas separation [3], as catalysts or catalyst supports [4], and as electrodes in supercapacitors [5]. A wide range of pore characteristics of ACs, such as the specific surface area, pore size distribution, and pore volume, can be controlled through the selection of raw materials and adjustment of the carbonization and activation conditions [6,7]. In particular, the activation process, which is divided into physical and chemical activation, is a key process to obtain ACs with highly developed pores. The advantages of ACs prepared by chemical activation include a higher specific surface area and higher yield, compared with those produced by physical activation [8–10]. For example, MAXSORB, an AC having one of the highest specific surface areas among commercial ACs and prepared by chemical activation using potassium hydroxide (KOH) as an activating agent, shows threefold higher Brunauer–Emmett–Teller surface area at the same yield of 50% than that by steam activation (physical activation) [11].

Many studies have been performed to clarify the reasons for superior pore development in chemically activated ACs. Marsh et al. described the activation process by KOH as involving two main mechanisms: (1) catalytic gasification of carbon into carbon monoxide and carbon dioxide, and (2) intercalation of potassium metal between graphitic layers, followed by rapid

removal [7]. Chemical reaction equations describing KOH and NaOH activations have also been proposed [11–13]. Structural investigations of the pore development mechanism of physical and chemical activations have been attempted using gas adsorption [14], X-ray diffraction [15–17], and transmission electron microscopy (TEM) [14,18–20]. Observation and analysis of pore structure of activated carbon fibers from various precursors, such as isotropic pitch, polyacrylonitrile, cellulose, phenol, and rayon, have been also carried out by using high-resolution TEM and image processing [21–23]. However, a direct comparison of the differences in the pore development mechanisms of these two activation processes is lacking, especially from a structural point of view.

The objective of this study was thus to elucidate the differences in the structural mechanisms of physical and chemical activation processes for AC preparation. Self-same phenol resin-based spherical carbon was used as the starting material because the activation degrees of produced ACs are largely influenced by raw materials and the carbonization conditions [6,7,12,24]. A new structural model, the microdomain structure model, which was recently proposed by some of the present authors [25], was adopted to resolve the AC structure. In this previous study, it has been revealed that each AC particle consists of numerous spherical microdomains, a basic structural unit, ~2–10 nm in diameter, by scanning tunneling microscopy (STM) observations [25]. Furthermore, unlike the conventional hierarchical pore structure model, in the microdomain structure model, micropores develop in each microdomain, and mesopores form between adjacent microdomains (i.e., in inter-microdomain space).

In this study, based on the microdomain structure model, a structural model to explain the difference in the pore development mechanisms between steam (physical) and KOH (chemical) activations is presented for the first time, through STM and scanning electron

microscopy (SEM) structural analyses of the shape and size changes of microdomains and particles together with observation of correlations between weight loss and the degree of pore development by different activation processes.

3.2. Experimental

3.2.1. Sample preparation

Spherical carbon (C6), prepared by the carbonization of a spherical phenol resin (BEAPS series, Asahi Yukizai Corporation, Japan) at 600℃ for 1 h in a flow of N_2, was used as the starting material. For AC preparation by physical activation, steam was used as the activating agent. C6 was heated to 700–900℃ at a ramping rate of 5℃ min^{-1} in N_2 flow (100 mL min^{-1}); the sample was held at the desired temperature for 1 h in a steam flow containing N_2 gas (relative humidity = 90%), which was produced by bubbling N_2 through boiling distilled water. After steam activation, the collected sample was dried at 150℃ for 12 h in a vacuum oven. AC preparation via chemical activation was performed using KOH (purity > 85.0%; Wako Pure Chemical Industries, Ltd., Japan) as an activating agent. The weight ratio of KOH/C6 was set to 6. The mixture of KOH and C6 was heat-treated at 700–900℃ at a rate of 5℃ min^{-1} and then held at the desired temperature for 1 h under N_2 flow (100 mL min^{-1}). After KOH activation, the remaining KOH and the salts formed during activation were removed by washing with HCl solution three times and deionized water once to adjust the pH to ~7. The prepared steam- and KOH-ACs were designated as C6Sx or C6Kx, respectively, where x indicates the number of the first digit of the activation temperature (x = 7, 8, or 9 as 700, 800, or 900℃, respectively).

3.2.2. Characterization

N_2 adsorption/desorption isotherms at 77 K were measured using a volumetric adsorption system (Belsorp-Max-S, BEL Japan Inc., Japan) to investigate porosity. Pore structural parameters were calculated from the αs-plot analyses of N_2 adsorption isotherms [26].

To observe changes in the microdomains via activation, STM observation of the prepared AC samples was carried out after heat treatment at 600℃ under a H2:Ar (1:4) atmosphere, to remove noise originating from heteroatoms. The STM images were acquired in constant current mode (current range: 0.1–1.0 nA; bias voltage: 0.1–2.0 V; scan frequency: 1–2 Hz) using an Agilent Technologies 5500 Scanning Probe Microscope (Toyo Corporation, Japan). The particle size was estimated using SEM (JSM-6700F, JEOL, Japan). The average microdomain and particle diameters were determined by counting 300 microdomains or particles in STM or SEM images, respectively.

3.3. Results and Discussion

N_2 adsorption/desorption isotherms of the parent spherical carbon (C6), and steam- or KOH-ACs are shown in Fig. 3-1. A rectangular adsorption isotherm indicated that C6 possessed ultramicropores only. Although both steam and KOH activations induced further pore development, a clear difference in the degree of pore development was observed. Table 3-1 shows pore structural parameters calculated from the αs-plot analyses of N_2 adsorption isotherms. By both steam and KOH activations, the total specific surface area increased, depending on the activation temperature. However, KOH-ACs showed higher total specific surface area than the steam-activated ones at the same activation temperature, as reported in the literature [8–11], which provides further evidence of effective pore development with KOH activation.

In Fig. 3-2, the relationship between weight loss and developed micropore volume by activation is shown. Here, the developed micropore volume was calculated as the difference in micropore volumes for C6 and each prepared AC. At an activation temperature, T_a, of 700℃, the weight loss by KOH activation (56%) was larger than that by steam activation (20%). On the other hand, the developed micropore volume of C6K7 was 1.21 $cm^3\ g^{-1}$, although C6S7 showed a negligibly small value (0.03 $cm^3\ g^{-1}$). This suggests that the large weight loss for KOH-AC was mainly due to pore development, whereas steam activation at T_a = 700℃ induced gasification of solid carbon (~20 wt%) without micropore development.
By applying a higher activation temperature, both steam and KOH activations gave rise to micropore formation. However, the rates of increase of micropore volume differed, depending on the activation type. In Fig. 3-2, the point corresponding to the C6K8 sample (prepared by KOH activation at T_a = 800℃) is located on an extrapolated line between the origin and C6K7 (the red broken line in Fig. 3-2), suggesting similar pore development

efficiency up to T_a = 800℃. For the steam-ACs, micropore development was nearly linear over the activation temperature range of 700–900℃ (the blue broken line in Fig. 3-2). The black dotted line in Fig. 3-2 is a displaced line of the red broken line for the KOH-ACs in the direction of abscissa axis. The difference in the slopes of the black dotted and red broken lines indicates the higher efficiency of pore development by KOH activation, compared with that by steam activation. The catalytic role of alkali metals in chemical activation was discussed in a previous study [7]. When KOH activation was carried out at T_a = 900℃, the micropore volume increased sharply without noticeable weight loss (4% reduction). This is because the pore development mechanism switched to potassium intercalation between graphene layers, as reported previously [7,8,11,13,27]. In addition, Fig. 3-3, and 3-4 show the relationship between weight loss and developed specific surface area, and relationship between weight loss and average pore size, respectively. The results of the Fig. 3-3, and 3-4 showed tendency of Fig. 3-2 result.

Fig. 3-5 and 3-6 show microdomain and particle images of C6 and KOH-ACs, respectively. Based on STM and SEM observations, the changes in the microdomain and particle sizes of KOH-ACs are summarized in Fig. 3-7. C6 was composed of spherical microdomains (average diameter: 6.1 nm), as shown in Fig. 3-5(a). After KOH activation, both the size and the shape of the microdomains were nearly unchanged, despite the remarkable increase in porosity (Fig. 3-5(b)–(d) and Fig. 3-7). Additionally, the spherical particle shape of KOH-AC was intact (Fig. 3-6), and the particle size of ~10 μm was nearly constant (Fig. 3-7). Regardless of the similar particle and microdomain sizes, the total specific surface area showed a substantial increase from 2189 $m^2 g^{-1}$ (C6K7) to 2878 $m^2 g^{-1}$ (C6K9), depending on the activation temperature. This indicates that micropores developed in the intra-microdomain region, while maintaining the size and shape of the particles and microdomains

in the case of KOH activation. That is, I confirmed that the weight loss observed for KOH-AC samples was almost solely due to pore development in intra-microdomain regions.

In contrast, steam activation induced a significant reduction in microdomain size, depending on the activation temperature, from 5.6 nm (C6S7) to 2.9 nm (C6S9), as shown in Fig. 3-7 and 3-8. Furthermore, the reduction in particle size with increasing activation temperature occurred (Fig. 3-7), while maintaining the original spherical shape as revealed in SEM images (Fig. 3-9). The oxidative reaction of steam progressed preferentially and violently at the outer surface of the carbon particles and microdomains, resulting in gasification of the outermost parts; thus, the sizes of both the particles and the microdomains decreased.

Fig. 3-10 shows the proposed model of the structural mechanism of pore development during physical and chemical activation processes, based on our findings. The microdomains of C6 were spherical, as revealed by STM observation. In the case of steam activation at T_a = 700℃, the microdomains located at the periphery of particles were completely gasified, giving rise to a reduction in particle size. At the same time, the size of the remaining microdomains became smaller whilst maintaining their spherical shape via preferential gasification at the outer surface. Here, gasification of a portion of the microdomains and particles resulted in weight loss of ~20%, but did not contribute to pore development. As the activation temperature rose, micropores started to develop in the microdomains; however, the efficiency was not as high as that for KOH activation. Again, the microdomains located at the periphery of the reduced particles, along with the outer surface of the remaining microdomains, were preferentially gasified; this further reduced the sizes of the particles and microdomains. Given the preferential gasification of microdomains at the periphery of carbon particles, in the case of steam activation, the remaining microdomains located at the core part

of the particles were likely to be activated inhomogeneously. In other words, micropores formed only for a portion of the remaining microdomains; the rest stayed intact. In contrast, KOH activation induced efficient and uniform pore development for microdomains consisting of carbon particles, without changing the sizes of the microdomains or particles; this was attributed to the catalytic role of the potassium species formed during activation [7,28].

Table 3-1. Pore structural parameters and activation yield of C6 and steam- and KOH-activated carbons. ("Reprinted from Journal of Carbon, 114 / 4015720288522, Doo-Won Kim, Hyun-Sig Kil, Koji Nakabayashi, Seong-Ho Yoon, Jin Miyawaki, Structural elucidation of physical and chemical activation mechanisms based on the microdomain structure model, 98-105, 2017, with permission from Elsevier.")

Sample	Specific surface area [m^2 g^{-1}]	Micropore volume [cm^3 g^{-1}]	Average pore width [nm]	Activation yield [%]
C6	655	0.24	0.73	-
C6S7	878	0.27	0.61	80
C6S8	1409	0.46	0.65	56
C6S9	2213	1.06	1.02	14
C6K7	2189	1.45	1.34	44
C6K8	2349	1.68	1.44	33
C6K9	2878	2.39	1.69	29

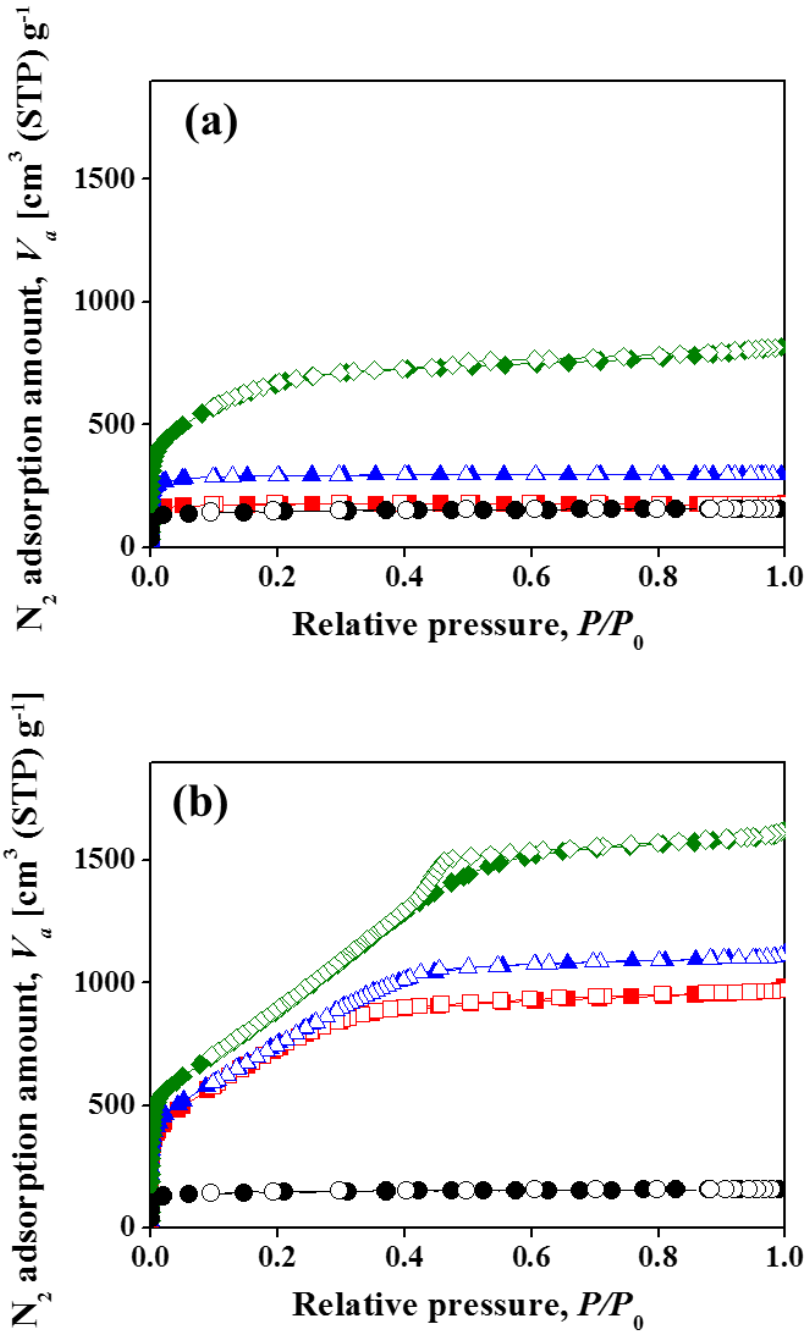

Fig. 3-1. N_2 adsorption/desorption isotherms at 77 K of C6 and (a) steam- and (b) KOH-activated carbons (ACs). The solid and open symbols denote adsorption and desorption isotherms, respectively. (Circle) C6; (square) C6S7 or C6K7; (triangle) C6S8 or C6K8; (diamond) C6S9 or C6K9. ("Reprinted from Journal of Carbon, 114 / 4015720288522, Doo-Won Kim, Hyun-Sig Kil, Koji Nakabayashi, Seong-Ho Yoon, Jin Miyawaki, Structural elucidation of physical and chemical activation mechanisms based on the microdomain structure model, 98-105, 2017, with permission from Elsevier.")

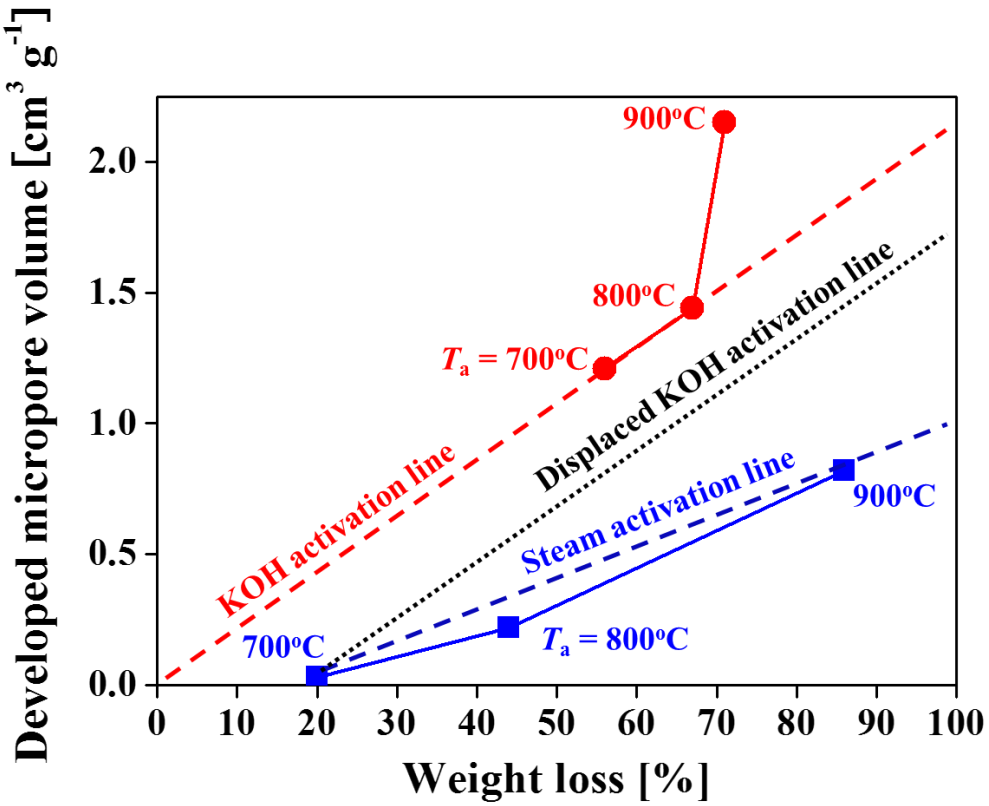

Fig. 3-2. Relationship between weight loss and developed micropore volume of (square) steam- and (circle) KOH-ACs prepared at different activation temperatures, T_a. ("Reprinted from Journal of Carbon, 114 / 4015720288522, Doo-Won Kim, Hyun-Sig Kil, Koji Nakabayashi, Seong-Ho Yoon, Jin Miyawaki, Structural elucidation of physical and chemical activation mechanisms based on the microdomain structure model, 98-105, 2017, with permission from Elsevier.")

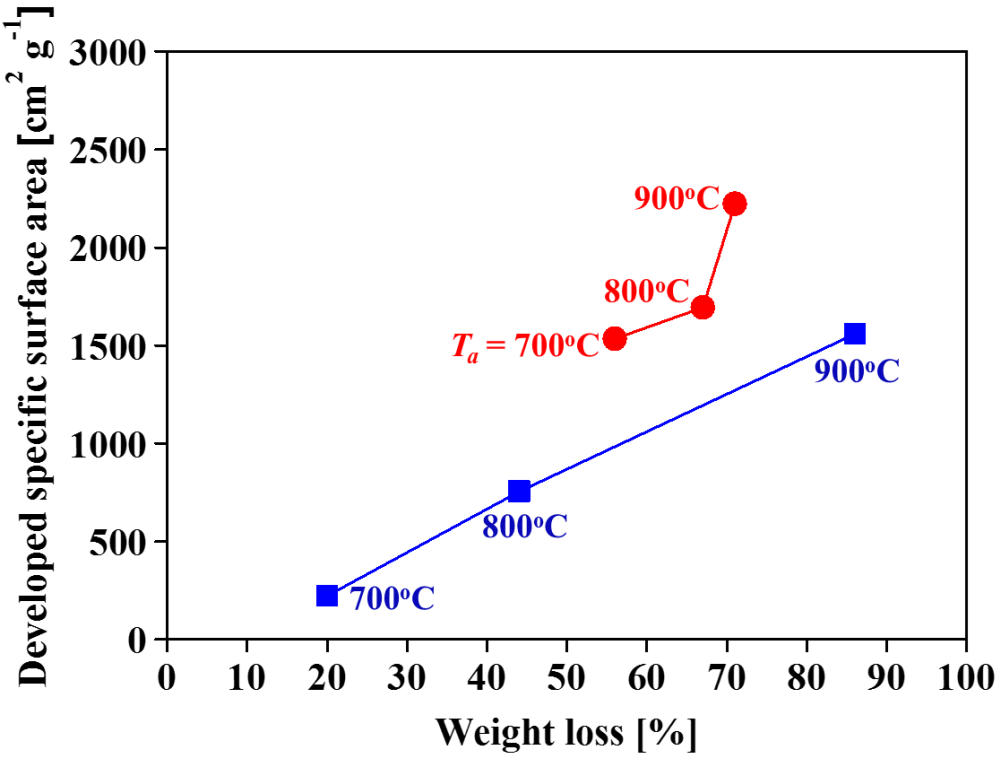

Fig. 3-3. Relationship between weight loss and developed specific surface area of (square) steam- and (circle) KOH-ACs prepared at different activation temperatures, T_a.

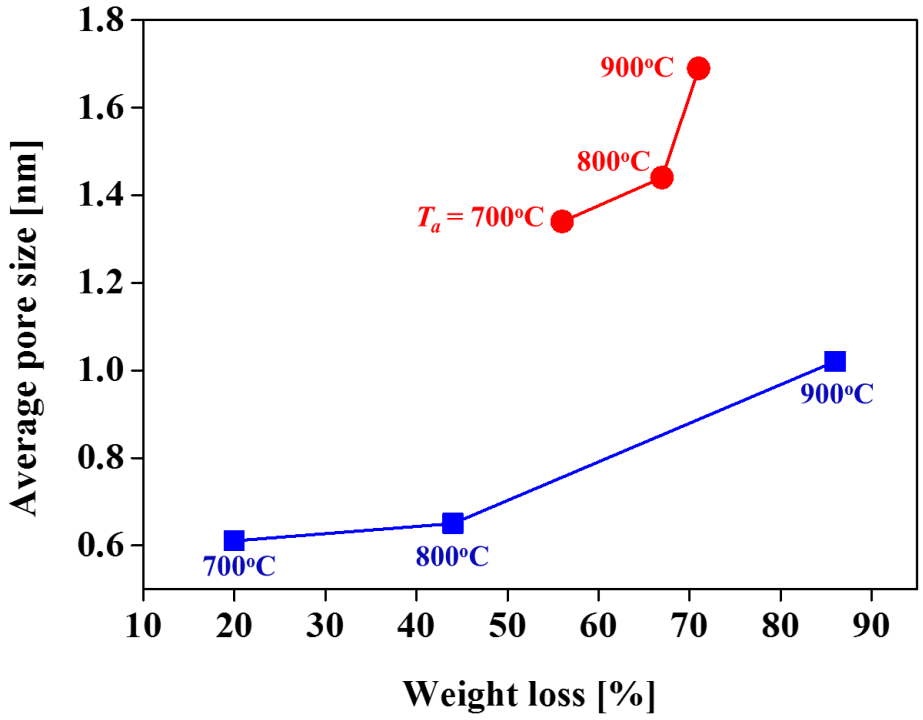

Fig. 3-4. Relationship between weight loss and average pore size of (square) steam- and (circle) KOH-ACs prepared at different activation temperatures, T_a.

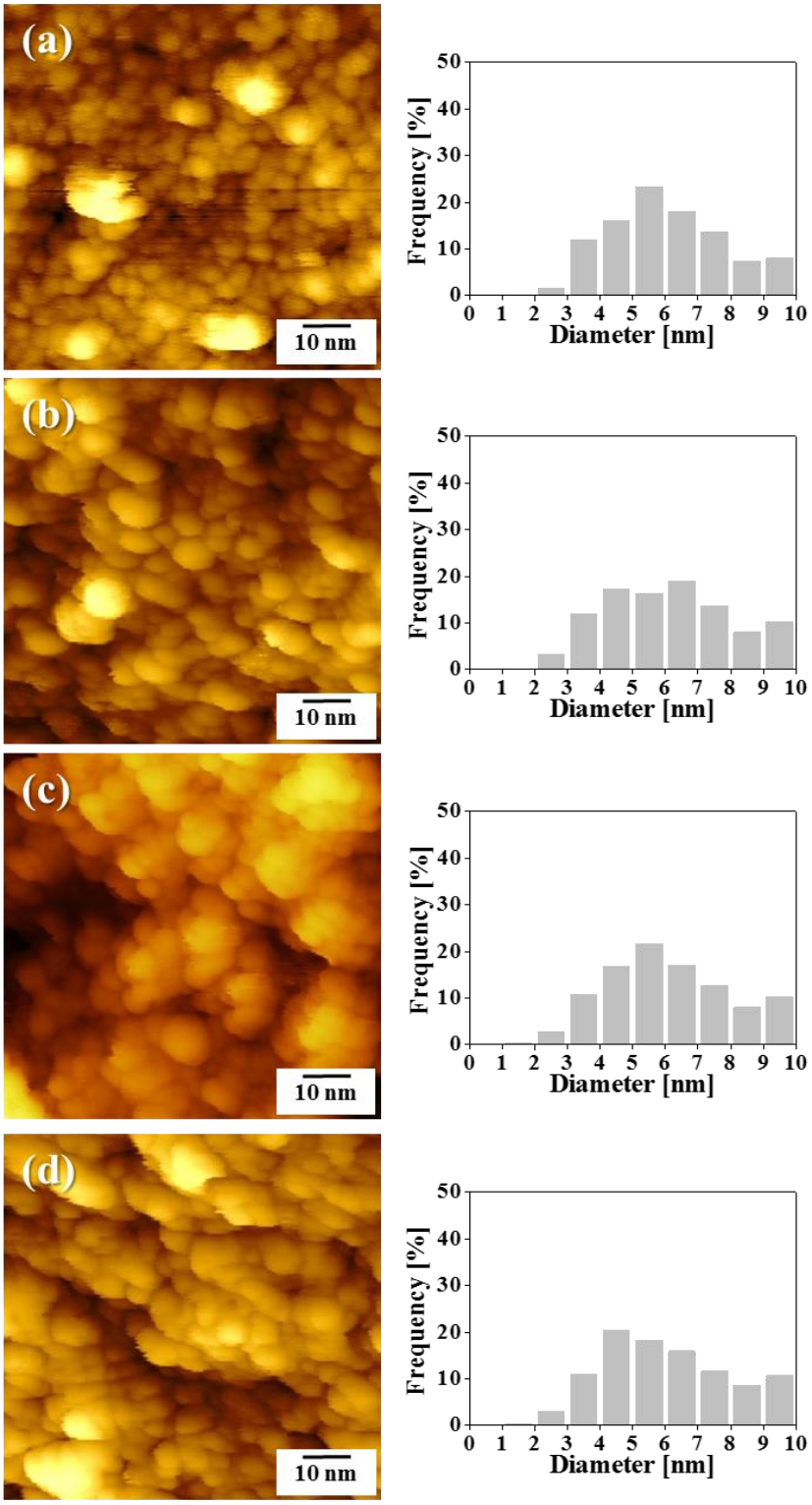

Fig. 3-5. Scanning tunneling microscopy (STM) images and microdomain size distributions of (a) C6, (b) C6K7, (c) C6K8, and (d) C6K9. ("Reprinted from Journal of Carbon, 114 / 4015720288522, Doo-Won Kim, Hyun-Sig Kil, Koji Nakabayashi, Seong-Ho Yoon, Jin Miyawaki, Structural elucidation of physical and chemical activation mechanisms based on the microdomain structure model, 98-105, 2017, with permission from Elsevier.")

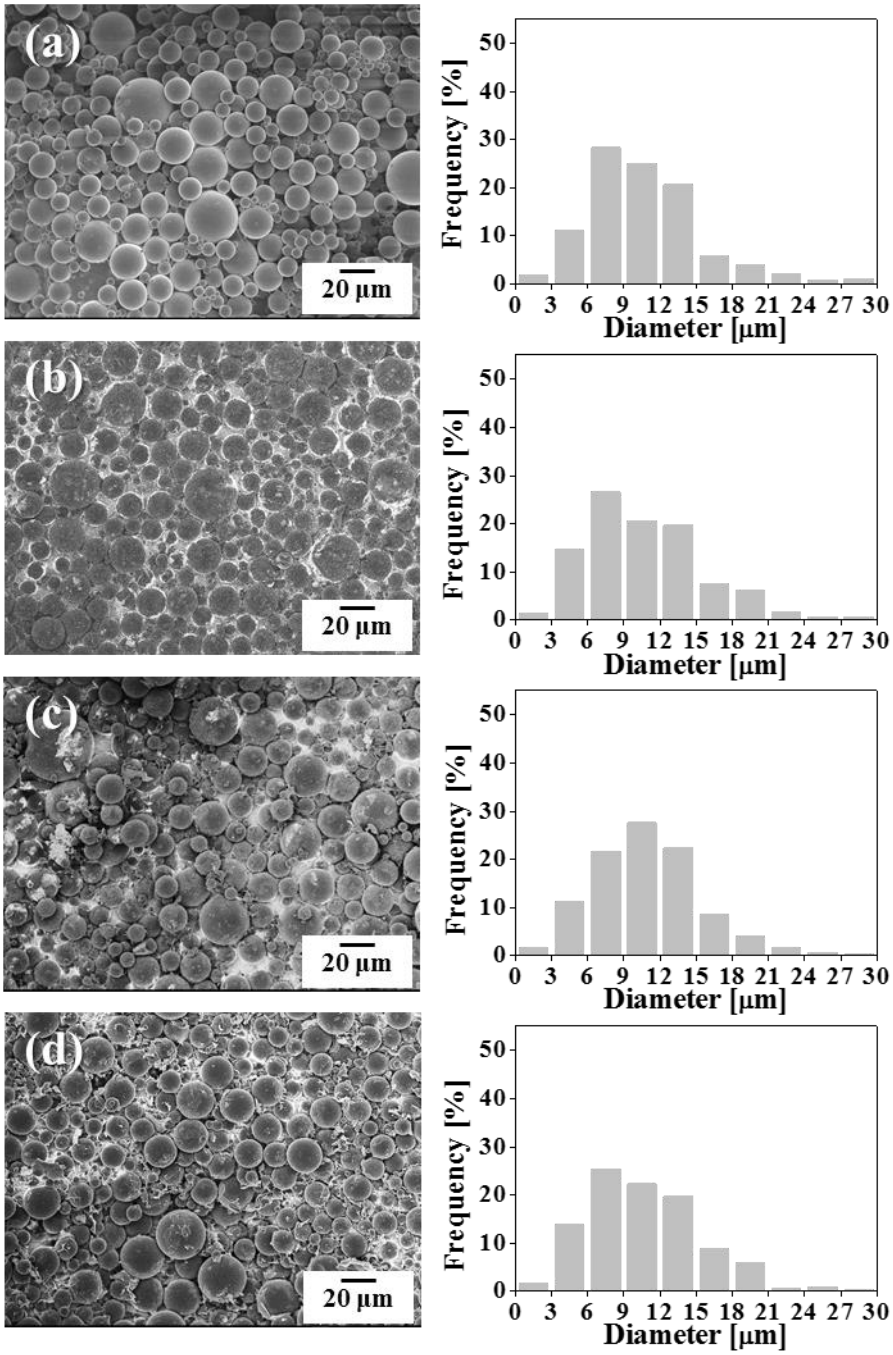

Fig. 3-6. Scanning electron microscopy (SEM) images and particle size distributions of (a) C6, (b) C6K7, (c) C6K8, and (d) C6K9. ("Reprinted from Journal of Carbon, 114 / 4015720288522, Doo-Won Kim, Hyun-Sig Kil, Koji Nakabayashi, Seong-Ho Yoon, Jin Miyawaki, Structural elucidation of physical and chemical activation mechanisms based on the microdomain structure model, 98-105, 2017, with permission from Elsevier.")

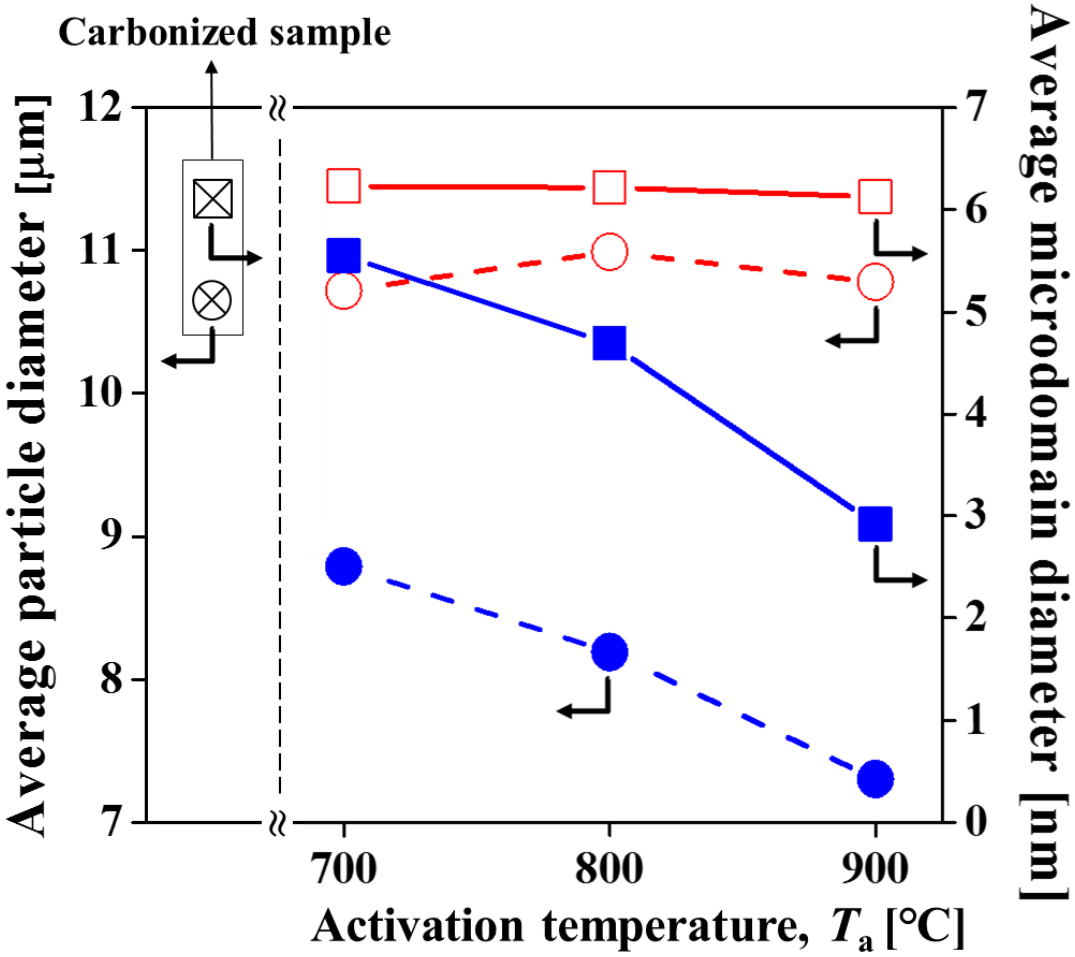

Fig. 3-7. Change of average sizes of (circle) particles and (square) microdomains by steam and KOH activations depending on activation temperature, T_a. The solid and open symbols denote steam- and KOH-ACs, respectively. ("Reprinted from Journal of Carbon, 114 / 4015720288522, Doo-Won Kim, Hyun-Sig Kil, Koji Nakabayashi, Seong-Ho Yoon, Jin Miyawaki, Structural elucidation of physical and chemical activation mechanisms based on the microdomain structure model, 98-105, 2017, with permission from Elsevier.")

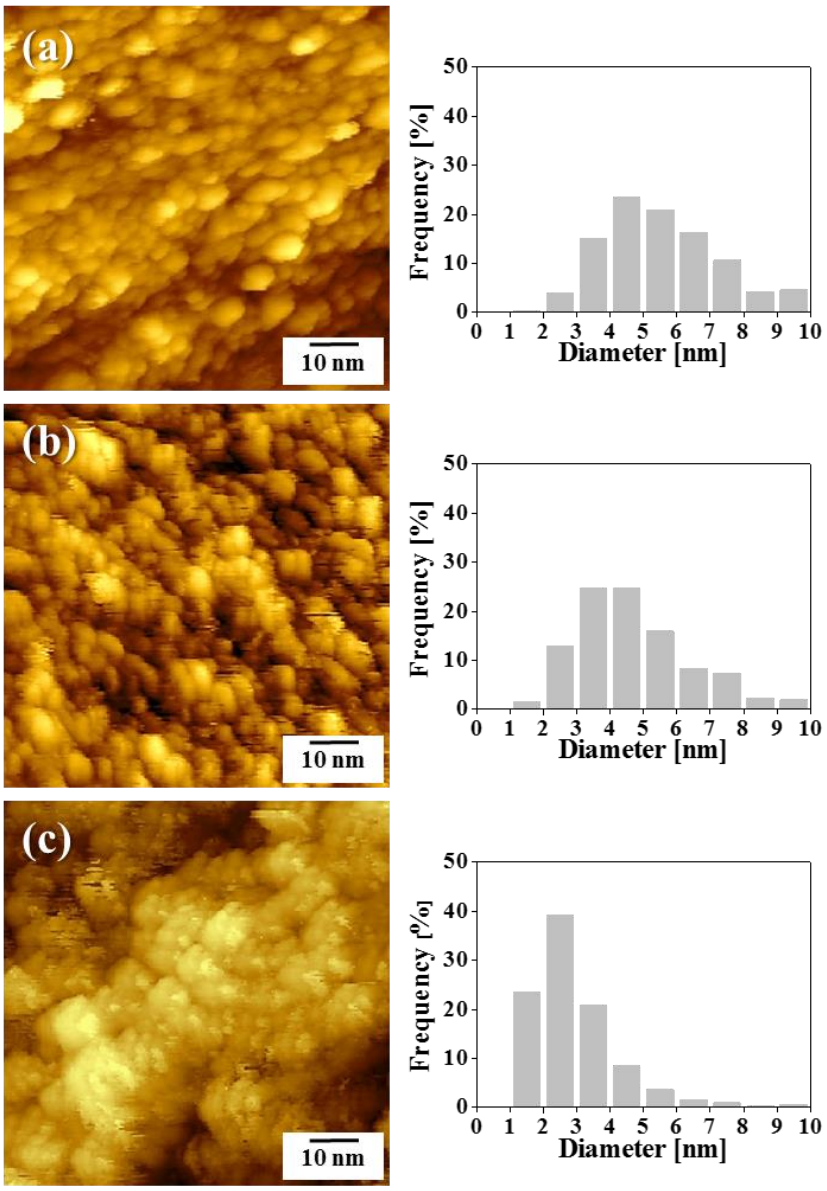

Fig. 3-8. STM images and microdomain size distributions of (a) C6S7, (b) C6S8, and (c) C6S9. ("Reprinted from Journal of Carbon, 114 / 4015720288522, Doo-Won Kim, Hyun-Sig Kil, Koji Nakabayashi, Seong-Ho Yoon, Jin Miyawaki, Structural elucidation of physical and chemical activation mechanisms based on the microdomain structure model, 98-105, 2017, with permission from Elsevier.")

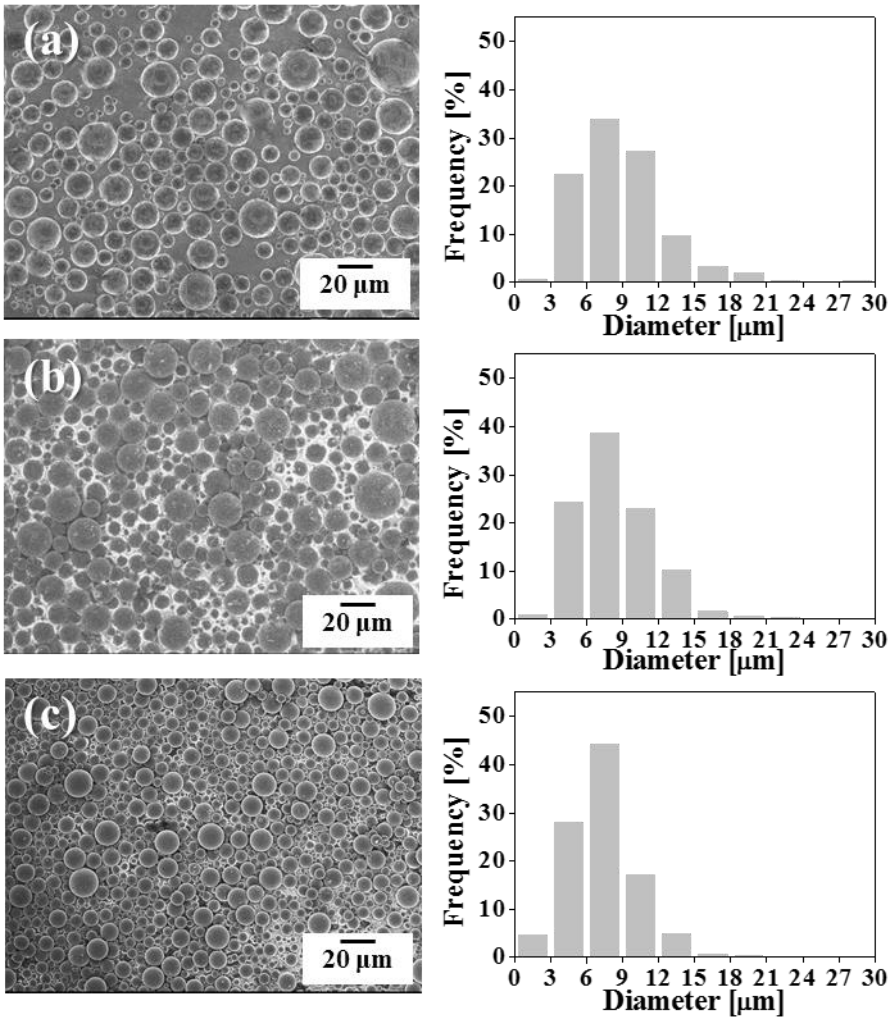

Fig. 3-9. SEM images and particle size distributions of (a) C6S7, (b) C6S8, and (c) C6S9. ("Reprinted from Journal of Carbon, 114 / 4015720288522, Doo-Won Kim, Hyun-Sig Kil, Koji Nakabayashi, Seong-Ho Yoon, Jin Miyawaki, Structural elucidation of physical and chemical activation mechanisms based on the microdomain structure model, 98-105, 2017, with permission from Elsevier.")

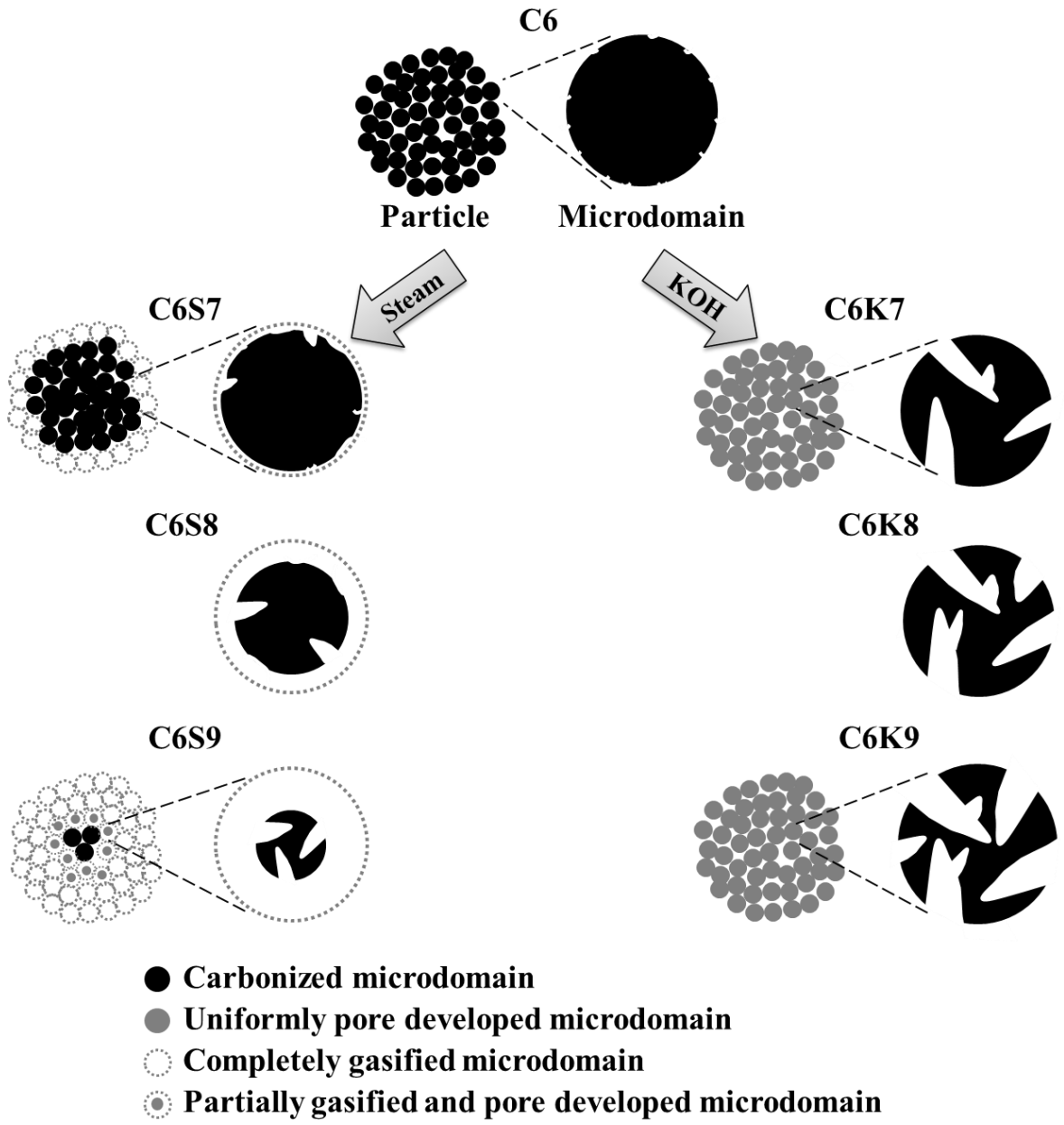

Fig. 3-10. Structural mechanism model of pore development for steam- and KOH-ACs. ("Reprinted from Journal of Carbon, 114 / 4015720288522, Doo-Won Kim, Hyun-Sig Kil, Koji Nakabayashi, Seong-Ho Yoon, Jin Miyawaki, Structural elucidation of physical and chemical activation mechanisms based on the microdomain structure model, 98-105, 2017, with permission from Elsevier.")

3.5. Conclusions

The different structural mechanisms of KOH and steam activations for AC preparation were explained based on the microdomain structure model. In the steam activation process, the sizes of both the microdomains and the particles decreased by inhomogeneous gasification; micropores formed only for a portion of the remaining microdomains. Thus, steam activation gave the lower yield and limited porosity. In contrast, KOH activation provided uniform pore development overall for microdomains consisting of carbon particles; the higher yield and superior pore development were attributed to the catalytic role of the potassium species produced during activation. The proposed structural mechanism model for pore development with physical and chemical activations is expected to serve as a guideline for developing ACs with highly controlled pore structures.

ACKNOWLEDGEMENTS

I appreciated that permission of reuse in a dissertation / thesis. Below, information about rights and permission is expressed.

"Reprinted from Journal of Carbon, 114 / 4015720288522, Doo-Won Kim, Hyun-Sig Kil, Koji Nakabayashi, Seong-Ho Yoon, Jin Miyawaki, Structural elucidation of physical and chemical activation mechanisms based on the microdomain structure model, 98-105, 2017, with permission from Elsevier."

References

[1] Radovic, L. R., Moreno-Castilla, C., and Rivera-Utrilla, J. "Carbon materials as adsorbents in aqueous solutions." *Chemistry and Physics of Carbon*, Vol. 27, Ed. Radovic LR. Marcel Dekker, New York, (2001): 227–406.

[2] Rodríguez-Reinoso, F. "Production and applications of activated carbons." *Handbook of Porous Solids*, Eds. Schüth F, Sing KSW, Weitkamp J. Wiley-VCH Verlag GmBH, Weiheim, Germany, (2002): 1766–1827.

[3] Kyotani, T. "Control of pore structure in carbon." *Carbon* **38** (2000): 269–286.

[4] Rodríguez-Reinoso, F. "The role of carbon materials in heterogeneous catalysis." *Carbon* **36** (1998): 159–175.

[5] Mastragostino, M., et al. "Electronically conducting polymers and activated carbon: electrode materials in supercapacitor technology." *Advanced Materials* **8** (1996): 331–334.

[6] Bansal, RC., Donnet, JB., Stoeckli, F. *Active Carbon*, Marcel Dekker, New York, (1998): 121–129.

[7] Marsh, H., and Rodríguez-Reinoso, F. *Activated Carbon*, Elsevier, Amsterdam, (2006): 350–358.

[8] Ahmadpour, A., and Do, D. D. "The preparation of active carbons from coal by chemical and physical activation." *Carbon* **34** (1996): 471–479.

[9] Maciá-Agulló, J. A., et al. "Activation of coal tar pitch carbon fibres: physical activation vs. chemical activation." *Carbon* **42** (2004): 1367–1370.

[10] Wu, F. C., Tseng, R. L., and Hu, C. C. "Comparisons of pore properties and adsorption performance of KOH-activated and steam-activated carbons." *Microporous and*

Mesoporous Materials **80** (2005): 95–106.

[11] Otowa, T., Ritsuo, T., and Masao, I. "Production and adsorption characteristics of MAXSORB: high-surface-area active carbon." *Gas Separation & Purification* **7** (1993): 241–245.

[12] Lillo-Ródenas, M. A., Cazorla-Amorós, D., and Linares-Solano, A. "Understanding chemical reactions between carbons and NaOH and KOH: an insight into the chemical activation mechanism." *Carbon* **41** (2003): 267–275.

[13] Romanos, J., et al. "Nanospace engineering of KOH activated carbon." *Nanotechnology* **23** (2011): 015401.

[14] Marsh, H., et al. "Carbons of high surface area. A study by adsorption and high resolution electron microscopy." *Carbon* **20** (1982): 419–426.

[15] Yoshizawa, N., et al. "XRD evaluation of CO_2 activation process of coal-and coconut shell-based carbons." *Fuel* **79** (2000): 1461–1466.

[16] Yoshizawa, N., et al. "XRD evaluation of KOH activation process and influence of coal rank." *Fuel* **81** (2002): 1717–1722.

[17] Dıaz-Terán, J., et al. "Study of chemical activation process of a lignocellulosic material with KOH by XPS and XRD." *Microporous and Mesoporous Materials* **60** (2003): 173–181.

[18] Huttepain, M., and Oberlin, A. "Microtexture of nongraphitizing carbons and TEM studies of some activated samples." *Carbon* **28** (1990): 103–111.

[19] Yoon, S. H., et al. "KOH activation of carbon nanofibers." *Carbon* **42** (2004): 1723–1729.

[20] Raymundo-Pinero, E., et al. "KOH and NaOH activation mechanisms of multiwalled carbon nanotubes with different structural organisation." *Carbon* **43** (2005): 786–795.

[21] Jibril, B. Y., et al. "Effects of feedstock pre-drying on carbonization of KOH-mixed bituminous coal in preparation of activated carbon." *Journal of Analytical and Applied Pyrolysis* **80** (2007): 277–282.

[22] Oshida, K., et al. "Analysis of pore structure of activated carbon fibers using high resolution transmission electron microscopy and image processing." *Journal of Materials Research* **10** (1995): 2507–2517.

[23] Endo, M., et al. "Visualized observation of pores in activated carbon fibers by HRTEM and combined image processor." *Supramolecular Science* **5** (1998): 261–266.

[24] Huang, Z. H., et al. "Pore structure and fractal characteristics of activated carbon fibers characterized by using HRTEM." *Journal of Colloid and Interface Science* **249** (2002): 453–457.

[25] Shiratori, N., et al. "Pore structure analysis of activated carbon fiber by microdomain-based model." *Langmuir* **25** (2009): 7631–7637.

[26] Kaneko, K., Ishii, C., and Ruike, M. "Origin of superhigh surface area and microcrystalline graphitic structures of activated carbons." *Carbon* **30** (1992): 1075–1088.

[27] Marsh, H., et al. "Formation of active carbons from cokes using potassium hydroxide." *Carbon* **22** (1984): 603–611.

[28] McKee, D. W. "Mechanisms of the alkali metal catalysed gasification of carbon." *Fuel* **62** (1983): 170–175.

Chapter 4

Highly graphitized carbon from non-graphitizable raw materials and its formation mechanism based on the domain theory

4.1. Introduction

Carbon materials are commonly classified into two categories, graphitizable and non-graphitizable, according to the degree of graphitization after heat treatment above 2800℃ (“graphitization”). Based on ‘conventional’ analyses, graphitizable carbon (GC) can be converted into a three-dimensional (3-D) graphitic structure (graphite) by the heat treatment of graphitization. At a temperature above 2800℃, a decrease in the interlayer spacing (d_{002}) and an increase in the interlayer thickness (L_c) occur. Graphitized GC is typically composed of homogeneous AB-type stacking of well-developed hexagonal carbon layers (a 3-D graphitic structure), such as single-crystal graphite [1]. In contrast to GC, non-graphitizable carbon (NGC) is usually difficult to convert to graphite, even after heat treatment above the graphitization temperature. Graphitized NGC is considered to be composed of random or heterogeneous stackings (ABC-type or others) of relatively small hexagonal carbon layers, which must have a rhombohedral crystal structure (turbostratic structure) [2,3]. From the stacking regularity of these hexagonal carbon layers, graphitized GC has higher electrical and thermal conductivities and mechanical properties than those of graphitized NGC due to the ease of electron transfer and reduction in defects [4,5]. Nevertheless, despite such X-ray diffraction (XRD)-based structural analyses of graphitized GC and NGC materials, a question

still remains as to what factor(s) is(are) decisive in determining GC and NGC properties in the precursor base *before* graphitization.

To date, it has been considered that structural differences in the carbon precursor depend primarily on the raw material. Thus, pitch, a carbon precursor that can be fabricated through liquid-phase carbonization of condensed aromatic hydrocarbons, usually belongs to the GCs. Such materials, e.g., mesophase pitch and needle coke (optically anisotropic coke with a needle-like oriented flow texture), are usually composed of large polycondensed aromatic compounds or condensed structures with somewhat developed stacking structures. In contrast, biomass, thermo-setting resins, and optically isotropic/mosaic cokes belong to the NGCs. However, optically isotropic and mosaic cokes are also composed of seemingly well-developed polycondensed aromatic compounds. So, what is the difference between needle coke and optically isotropic coke?

Franklin first reported a relationship between the molecular structure of the carbon precursor and the graphitization behavior of GCs and NGCs, based on XRD analyses of various carbonaceous materials in 1951 [1]; in the study, precursor molecular and graphitized structural models of GCs and NGCs in two dimensions were proposed [6]. In the Franklin model, GCs show an oriented molecular structure (parallel and regular), whereas the molecular orientation of NGCs is essentially random. The key problem with the Franklin model is the absence of size quantification. Shiraishi first suggested a 3-D shell model of graphitized NGC (graphitized glassy carbon) from a structural analysis with transmission electron microscopy (TEM) [7]. In this shell model, well-developed hexagonal carbon layers are composed of concentric cell-like structures, around 5 nm in diameter.

Our group suggested a 3-D structural model of mesophase pitch-based carbon fiber (MPCF) from combined analyses with scanning electron microscopy (SEM), scanning tunneling

microscopy (STM), and TEM [8-10]. We first proposed microdomain and domain structural units that could restrict the magnitude of crystalline development in the graphitized GCs. In MPCF, we propose that domains, composed of microdomains (quasi-aligned molecular assembly units) in the mesophase pitch are closely packed, being aligned but incompletely connected; this configuration restricts the graphitic degree [9,10]. In particular, the oxidation of molecules in the stabilization process may explain the incomplete sintered connection of such closely packed domains [8, 9]. Thus, the degree of graphitization of MPCF is restricted to a domain size of less than 70 nm in L_a (110), even after graphitization. We also improved the domain-based structural analysis of carbon material into a hierarchical domain structural analysis [10]. Hierarchical domain structural analysis of carbon material can be explained as the serial formation of carbon structures from molecules (e.g., a hexagonal carbon layer), molecular assemblies (e.g., stacked units), microdomains (an assembly of stacked units), domains (an assembly of microdomains), and bulk (an assembly of domains). Based on this hierarchical domain structural analysis, we define a GC as being composed of domains that have partially merged microdomains, whereas a NGC is composed of domains that have few or no merged (almost independent) microdomains. Thus, in a hierarchical domain structural analysis, GCs have larger domain sizes, of 20–70 nm, composed of partially merged microdomains, whereas NGCs have similar or slightly larger domains with microdomains of 5–15 nm.

Recently, we applied such a hierarchical domain structural analysis to the pore formation mechanism in activated carbon fibers [11]; an examination of the relationship between the physical properties and the structures of polyacrylonitrile (PAN) and pitch-based carbon fibers [12] was conducted. If our novel structural analysis is correct, then we would expect to be able to convert NGCs to GCs through modifying the merging assembly of microdomains

and domain size, which ultimately means that we should be able to obtain a well-developed graphite structure after graphitization with a NGC precursor.

Several methods, such as catalytic graphitization and graphitization under tension, have been tried in an attempt to obtain a graphite structure from NGC precursors. Catalytic graphitization is one method to convert NGCs to a highly developed graphite structure through graphitization. Oya *et al*. described catalytic graphitization using many metal compounds [13,14]. The mechanism of catalytic graphitization has been explained as the dissolution-precipitation of carbon atoms on a metal surface or the formation and decomposition of metal carbides, but it remains unclear [15]. However, the commercial application of catalytic graphitization has been difficult due to the partial graphitic conversion on the catalyst surface and the problem of catalyst metal contamination. Graphitization under stress is another method that can accelerate the graphitization of NGCs, such as cellulose-based fiber, but it is too costly for widespread use [16-18]. Moreover, a combined technique of catalytic graphitization under pressure [19,20] did increase the degree of graphitization but its effect was limited.

In this study, we had two objectives: (1) to find a novel method to convert NGC into GC, and (2) to analyze the conversion mechanism, based on the novel hierarchical domain structural analysis. Previously, we have reported that extreme potassium hydroxide (KOH) treatment in the activation reaction could destroy the unit structure of carbon nanofibers [21]. Thus, alkaline salt treatment is considered to be a suitable method for modifying the merging assembly of microdomains and the domain structure without catalytic graphitization and under tension. Moreover, it does not involve catalytic metals, such as nickel, boron, zinc, and iron [13,14]. Sodium hydroxide (NaOH) was selected as the domain-modifying agent.

Thermo-set phenol resin-based beads, carbonized at 600℃, were selected as a typical NGC precursor.

4.2. Experimental

4.2.1. Materials and modification of NGC precursor into GC

Thermo-set spherical phenol resin-based beads (SPRs; BEAPS series, Asahi Yukizai Corporation, Japan) were used as a raw material for the non-graphitizable precursor. The SPRs had an average particle size of 17 μm and a spherical shape.

SPRs were treated at 600℃ for 1 h at a heating rate of 5℃ min^{-1} under a N_2 flow. To modify the domain structure of the pre-heat-treated SPRs, they were further heat-treated with six times the weight of NaOH (purity > 97.0%; Wako Pure Chemical Industries, Ltd., Japan) at 900℃ for 1 h using a heating rate of 5℃ min^{-1} under a N_2 flow. After heat treatment with NaOH, the remaining NaOH was washed away with 10% HCl aqueous solution and deionized water until the wash water was at pH 7. After washing, the collected sample was dried at 100℃ for 3 h in an air oven and dried again at 150℃ for 12 h in a vacuum oven.

To obtain graphitized samples, pre-heat-treated SPRs and the NaOH-treated samples were further heat-treated at 2800℃ for 10 min under an Ar atmosphere, in a horizontal tubular-type graphitization furnace (Kurata Giken Co., Ltd., Japan). Graphitized needle and isotropic cokes (from a Japanese company) were also produced with the same graphitization process to observe the domain sizes and shapes of typical graphitized GC and NGC, respectively. Table 1 summarizes the sample codes and the preparation conditions.

4.2.2. Characterization of samples

XRD analyses were performed using a RINT 2200 diffractometer (Rigaku, Japan) with Cu-Kα radiation (wavelength, λ: 0.15406 nm), generated at 40 kV and 30 mA. Scans were

performed at 1.0° min^{-1} for 2θ values between 10° and 90°. Crystallographic parameters (d_{002}, $L_c(002)$, and $L_a(110)$) were calculated using the Bragg and Scherrer equations [22,23].

Raman spectra were obtained with a Raman spectrometer (NRS-3000, JASCO, Japan) using a 532-nm Ar-ion laser as the excitation source. The first-order Raman spectra of samples were deconvoluted using four disordered (D1, D2, D3, and D4) bands and one ordered (G) band combination.

The macro-morphology of samples was observed using high-resolution SEM (JFM-6700F, JEOL, Japan). The mesoscopic morphology of samples was observed using STM (Agilent Technologies 5500 Scanning Probe Microscope, Toyo Corporation, Japan). Images were acquired in constant current mode (current range: 0.1–1.0 nA, bias voltage: 0.1–2.0 V, scan frequency: 1–2 Hz).

4.3. Results and discussion

4.3.1. Hierarchical domain structural analysis of graphitized needle and isotropic cokes

Fig. 4-1 shows STM images of graphitized needle coke (graphitizable coke) and graphitized isotropic coke (non-graphitizable coke), which were heat-treated at 2800℃ for 10 min. The graphitized needle coke showed 20–70-nm one-directionally arranged structural units (domains) that were composed of small microdomains of size < 10 nm, as shown in Fig. 4-1(a). The microdomain and domain structures of the graphitized needle coke looked similar to those of MPCF [8].

However, the graphitized isotropic coke (non-graphitizable coke) showed a smaller domain structure, < 10 nm, with microdomains of ~5 nm (Fig. 4-1(b)). From these results, we confirmed that the size and shape of the domain structure, determined by the assembly of microdomains, was a decisive factor in the properties of GCs and NGCs.

Fig. 4-2 shows revised hierarchical structural models of GC and NGC, based on the STM images of the graphitized needle and isotropic cokes (Fig. 4-1). In this model, the alignment of stacked units in the merged microdomains in GC was corrected and the graphitized domain structures of GC and NGC were newly added to the previously proposed models [10].

4.3.2. Elemental composition of raw and prepared samples

Elemental analyses were carried out using a CHN analyzer (MT-5, Yanako, Japan). The averaged assay of oxygen content ($O_{diff.}$) was determined by subtracting the sum of the contents of carbon, hydrogen, and nitrogen from 100%. The elemental compositions of the raw material (SPR), the pre-heated treated carbon (SPR-C6), and the NaOH-treated SPR-C6

(SPR-C6A9) are included in Table 4-1 to assess the remaining sodium. The raw material showed relatively high oxygen and hydrogen contents due to the chemical structure of the phenolic resin. After pre-heat treatment, the carbon content increased, from 75.20% to 90.45%, due to the conversion of organic substances into carbonaceous materials. Additionally, the SPR and SPR-C6 showed trace of ash content, indicating that the starting material did not contain metal impurities. SPR-C6A9 was composed of carbon, hydroxide, nitrogen, oxygen, and ash, at 95.18%, 0.22%, 0.26%, 4.34%, and 0.00%, respectively. The ash content of 0.00% indicated that remaining potassium had been removed completely by the HCl washing. Consequently, NaOH treatment was used to change the domain structure, not catalytic graphitization.

4.3.3. Characterization of graphitization properties of the samples

Fig. 4-3 shows the XRD profiles of SPR-C6, SPR-C6A9, and graphitized SPR-C6G and SPR-C6A9G. For SPR-C6, background uptake, indicated by small-angle scattering associated with the undeveloped carbon structure, and broad and obscure peaks at (002), (10), and (110) diffractions were observed, confirming that SPR-C6 was a typical NGC precursor. Although the diffraction peaks became much clearer after the heat treatment of SPR-C6 at 2800℃, the broadness and the peak position, at a lower angle than that of graphite, indicated a low degree of graphitization in the phenol resin-derived carbon.

In comparison with SPR-C6, SPR-C6A9 showed relatively developed (002) and (10) peaks, with a weakened background, due to the thermal treatment at 900℃ with the NaOH salt. The SPR-C6A9G exhibited five well-developed, distinctive diffraction peaks, which were assigned as (002), (100), (101), (004), and (110).

Values of the interlayer spacing (d_{002}), the thickness of stacking ($L_c(002)$), and the width of the hexagonal carbon layer ($L_a(110)$) of SPR-C6, SPR-C6A9, and graphitized SPR-C6G and SPR-C6A9G are summarized in Table 4-2. It was difficult to evaluate the crystalline parameters of SPR-C6 due to its amorphous nature. Graphitized SPR-C6 (SPR-C6G) showed values of $L_c(002)$, $L_a(110)$, and d_{002} of 4.7 nm, 16.9 nm, and 0.3424 nm, respectively, indicating that SPR-C6 was an ideal NGC precursor. In contrast, NaOH-treated SPR-C6 (SPR-C6A9) showed values of $L_c(002)$ and d_{002} of 14.2 nm and 0.3404 nm, respectively, indicating that SPR-C6A6 had already been converted to a graphitic structure through the extreme NaOH treatment. However, the $L_a(110)$ of SPR-C6A9 was difficult to evaluate due to the weak peak. Moreover, for the graphitized SPR-C6A9 (SPR-C6A9G), the values of $L_c(002)$, $L_a(110)$, and d_{002} were 31.8 nm, 52.3 nm, and 0.3368 nm, respectively, indicating that SPR-C6 had a well-developed graphitic structure.

In Fig. 4-4, representative first-order Raman spectra for each sample are compared. All samples showed the well-known D1 (disorder) band at ~1350 cm^{-1} and the G (graphite) band at ~1580 cm^{-1}. In the case of SPR-C6, many disordered peaks were also observed, at ~1200 (D4), ~1500 (D3), and ~1620 cm^{-1} (D2), which were attributed to sp^3 carbon or impurities, amorphous carbon, and disordered carbon, respectively [24]. The strong D1 band indicated that SPR-C6 and SPR-C6G had low degrees of graphitization, large amounts of disordered structures, and many defects, all characteristics of NGCs. However, SPR-C6A9 displayed a weak D1 band and a prominent G band. The disappearance or weakening of D bands indicated the destruction of the non-graphitizable structure due to the NaOH-treatment. Additionally, the relative increase in the G peak intensity indicated structural change. In Fig. 4-4(d), SPR-C6A9G showed a sharp and prominent G-band peak, and very weak D1- and D2-band peaks. Also, apart from the D1 band, the other D bands disappeared completely,

confirming that SPR-C6A9 was successfully converted to a GC precursor through heat treatment with NaOH at 900℃. After graphitization, SPR-C6A9 showed a well-developed, highly graphitized structure due to re-arrangement of the structure.

Table 4-2 also summarizes the calculated crystalline parameters from Raman spectroscopy. The D/G peak intensity ratio (I_D/I_G) and full-width at half-maximum of G band (G-FWHM), which can be used as indices of the degree of graphitization, were calculated from the deconvoluted peaks of the Raman spectra [25]. The I_D/I_G values of SPR-C6 and SPR-C6G were 1.08 and 0.99, respectively, showing characteristics of NGC. The values of G-FWHM for SPR-C6 and SPR-C6G were 61.7 cm^{-1} and 43.2 cm^{-1}, respectively, indicating that the degree of graphitization for SPR-C6 was restricted. Compared with these results, the values of I_D/I_G and G-FWHM for NaOH-treated SPR-C6 (SPR-C6A9) and its graphitized form (SPR-C6A9G) were 0.41 and 0.06, and 31.3 cm^{-1} and 24.8 cm^{-1}, respectively, indicating that the NaOH treatment of SPR-C6 was successful in converting the NGC of SPR-C6 to GC in SPR-C6A9. In particular, graphitized SPR-C6A9 (SPR-C6A9G) showed a similar value of G-FWHM to natural graphite.

From XRD and Raman spectroscopic results, it was confirmed that the NGC structure had changed only slightly, despite the high heat-treatment at 2800℃. However, after NaOH treatment, SPR-C6, an ideal NGC, was transformed to SPR-C6A9, a GC, indicating that the NaOH treatment was effective in converting NGC to GC. In particular, graphitized SPR-C6A9 (SPR-C6A9G) showed a well-developed graphite structure without relying on catalytic graphitization.

4.3.4. Macroscopic morphological changes in SPR-C6, SPR-C6A9, and their graphitized forms

Macro-morphological observations of SPR-C6, SPR-C6A9, and their graphitized forms were made using high-resolution SEM. Fig. 4-5 shows the SEM images of SPR-C6, SPR-C6A9, and the graphitized forms. SPR-C6 maintained the spherical shape with very smooth surfaces, as shown in Fig. 4-5(a). After graphitization, SPR-C6G maintained a spherical shape and a smooth surface (Fig. 4-5(b)). However, NaOH treatment caused marked changes in the morphologies of SPR-C6A9 and SPR-C6A9G. In Fig. 4-5(c), SPR-C6A9 showed completely different morphological shapes, composed of spherical shells with wrinkled surfaces. SPR-C6A9G maintained the same form despite graphitization (Fig. 4-5(d)). From Fig. 4-5(c) and (d), the NaOH treatment of SPR-C6 above 850℃ was expected to progress the conversion of SPR-C6 into the partially oriented stacked hexagonal carbon exfoliated sheets, although some of the SPR-C6 remained in an unconverted form. From SEM images, the conversion and the creation of the different morphological particles of SPR-C6 to SPR-C6A9 were observed clearly. It was still difficult to assess whether the morphological conversion of SPR-C6 to SPR-C6A occurred via only a gasification reaction, as SPR-C6 can be gasified but not deposited with the creation of shell-like particles, composed of well-developed hexagonal carbon sheet shell-like particles on the surface of or within the molten NaOH salt.

4.3.5. Mesoscopic morphological changes in SPR-C6, SPR-C6A9 and their graphitized forms

Mesoscopic morphological changes in samples were evaluated from STM observations. Fig. 4-6 shows STM images of SPR-C6 and SPR-C6A9 and their graphitized forms. In Fig. 4-6(a), a microdomain of 2–5 nm with an independent structure of SPR-C6 was confirmed. SPR-C6 showed relatively small domains, of 2–13 nm, which matched well with the size of

the NGC domains. The graphitized SPR-C6G showed slightly larger domains, 5–18 nm in size, than SPR-C6, indicating that the assembled states of the microdomains of SPR-C6 should be somewhat co-shared with the other. The crystalline parameters and morphologies of SPR-C6 and its graphitized form were in good agreement (Table 4-2, Fig. 4-6) indicating that morphological size and connection type are the most decisive factors in restricting graphitization.

STM images of SPR-C6A9 and its graphitized form, SPR-C6A9G, showed distinct differences in their domain morphologies (Fig. 4-6(c), (d)). Compared with the domain morphology of SPR-C6, which had small round domains, 2–13 nm in size, that of SPR-C6A9 illustrated much larger, oriented, arranged domains, 2–18 nm in size, composed of newly created microdomains that had merged.

The connection states of the microdomains in SPR-C6 and SPR-C6A9 appeared to be markedly different, as shown in Fig. 4-6(a) and (c). The microdomains of SPR-C6 looked round in shape, with distinct boundaries from each other, indicating that the microdomains of SPR-C6 were relatively independent, without significant merging. In contrast, those of SPR-C6A9 still showed boundaries of microdomains, but were largely indistinguishable. The domain size in SPR-C6A9 was considerably larger, ~18 nm; moreover, the domains were mostly oriented in one direction, indicating that the microdomains were modified in terms of the connection state, with some merging due to the NaOH treatment. The modified domains of SPR-C6A9 showed a similar structural morphology to those of needle coke and MPCF. After graphitization (Fig. 4-6(d)), the domains of SPR-C6A9G showed well-developed and large structures. Moreover, the boundaries of the microdomains were nearly indistinguishable. Table 4-3 summarizes the microdomain and domain sizes and shapes.

From the STM results, the NaOH treatment of SPR-C6 at 900℃ appears to have converted the connection state of the microdomains, making them merge with each other and become more oriented, typical of the microdomain structure of GCs.

4.3.6. Conjecturing the conversion mechanism of NGC domain into GC domain

By applying a higher temperature, the treatment with alkaline salt such as KOH and NaOH usually gives rise to abundant micropore formation [26, 27]. However, the rate of increase of micropore volume differed, depending on the activation temperature [27]. Activation in the temperature (T_a) range from 700°C to 800°C shows a similar pore development efficiency. When the activation is carried out at 900°C, the micropore volume increased sharply without noticeable weight loss (4% reduction) because the pore development mechanism switched to sodium intercalation between graphene layers, as reported previously [27]. At the same time, CO_2 emission might also take place, because T_a = 900°C was high enough for a decomposition of sodium carbonate (Na_2CO_3), which was formed by a reaction between NaOH and solid carbon, to give CO_2 and Na_2O. We guessed such expansion of graphene layers and rapid release of CO_2 might be reason for destroying the microdomains of SPR-C6. The formation of larger domains which might be composed of merged microdomains in SPR-C6A9 is still not clear. We are continuing to investigate the exact formation mechanism of GC domain.

4.3.7. Structural modeling of NGC and GC based on the microdomain structure

In Fig. 4-7, we propose mesoscopic structural models of SPR-C6, SPR-C6A9, and their graphitized forms based on the revised hierarchical domain analysis. The microdomains of

SPR-C6 were composed of typical round shapes, with a size of about 2–5 nm and were independent. The domains of SPR-C6 were slightly larger, up to 13 nm compared with the microdomains, and were nearly independent; however, some parts of the microdomains had merged slightly. The graphitized SPR-C6G showed larger domains, 5–18 nm, due to the graphitization with partially merged microdomains. From comparisons of STM images and XRD data of SPR-C6 and SPR-C6G, we confirmed that SPR-C6 was a NGC precursor. The NGC model was reflected in the round and partially merged shapes; also, non-graphitizable structural characteristics were apparent on the inside of the round and partially merged shapes. When graphitization proceeded without additional treatment, microdomains of NGC were merged, while maintaining a round shape. This merged structure was due to the growth of crystallite sizes (L_a and L_c), as shown in the XRD results, but the internal structure was non-graphitizable and nano-sized, as the Raman results showed.

In contrast, the domains of SPR-C6A9 were composed of typical merged microdomains, with sizes up to 18 nm, which were mostly newly created by the merging of microdomains. The domains of SPR-C6A9 showed larger sizes, up to 18 nm, compared with those of the microdomains, because they had almost merged. It should be noted that the domains an elongated shape of SPR-C6A9 were mostly aligned in one direction. The graphitized SPR-C6A9G showed much larger domains, with sizes over 50 nm, which were due to the graphitization of the merged microdomains. From comparisons of STM images and XRD data for SPR-C6A9 and SPR-C6A9G, we confirmed that SPR-C6A9 was a GC precursor. The GC model was reflected in the connected microdomains and domain shapes. When graphitization proceeded, the microdomains of GC merged substantially, with growth in the domain size. These merged structures were reflected in the growth of the crystalline parameters (L_a and L_c), as shown in the XRD results. The newly created domains in SPR-

C6A9, composed of merged microdomains due to the NaOH treatment, can be connected through their unconstrained structure and developed as a highly GC structure.

Table 4-1. Designation of prepared sample with main features and preparation parameters.

Designation	Main features	Heat treatment condition			
		Heating rate [℃]	Temperature [℃]	Holding time [min]	Atmosphere
SPR	Spherical phenol resin (SPR) Non-graphitizable raw material Average particle size : 17 μm Elemental composition of carbon, hydroxide, nitrogen, oxygen, and ash, at 75.20, 5.69, 0.07, 19.04, and 0.00%, respectively	-	-	-	-
SPR-C6	Carbonized SPR Non-graphitizable carbon material Spherical shape Elemental composition of carbon, hydroxide, nitrogen, oxygen, and ash, at 90.45, 3.35, 0.02, 6.18, and 0.00%, respectively	5	600	60	Nitrogen
SPR-C6G	Graphitized SPR-C6 Non-graphitizable carbon material Spherical shape	20	2800	10	Argon
SPR-C6A9	Activated SPR-C6 with NaOH Structure-destroyed carbon materials Core-shell separated shape Elemental composition of carbon, hydroxide, nitrogen, oxygen, and ash, at 95.18, 0.22, 0.26, 4.34, and 0.00%, respectively	5	900	60	Nitrogen
SPR-C6A9G	Graphitized SPR-C6A9 Graphitizable carbon material Core-shell separated shape	20	2800	10	Argon

Table 4-2. X-ray diffraction crystalline parameters, and full width at half maximum intensity of G band (G-FWHM) and relative intensities of D band to that of G band I_D/I_G in the first-order Raman spectra.

Sample	X-ray diffraction			Raman			
	L_c (002) [nm]	L_a (110) [nm]	d_{002} [nm]	I_D/I_G	G band position [cm^{-1}]	D band position [cm^{-1}]	G-FWHM [cm^{-1}]
SPR-C6	Not measurable (< 1)	Not measurable (< 1)	Not measurable	1.08	1582	1356	61.7
SPR-C6G	4.7	16.9	0.3424	0.99	1580	1345	43.2
SPR-C6A9	14.2	Not measurable (< 1)	0.3404	0.41	1580	1348	31.3
SPR-C6A9G	31.8	52.3	0.3368	0.06	1580	1350	24.8
SP-20 (nature graphite)	> 100	> 100	0.3356	0.14	1584	1353	19.1

Table 4-3. Summary of microdomain, domain, and these shapes.

Sample	STM observation		XRD analysis		Shape
	Microdomain size [nm]	Domain size [nm]	L_c (002) [nm]	L_a (110) [nm]	
SPR-C6	2 - 5	2 – 13	Not measurable (< 1)	Not measurable (< 1)	Spherical shape (Predominantly independent)
SPR-C6G	2- 10	5 - 18	4.7	16.9	Spherical shape (Predominantly independent) Elongated shape (Partially merging)
SPR-C6A9	2 - 5	2 - 18	14.2	Not measurable (< 1)	Elongated shape (Predominantly merging) Spherical shape (Partially independent)
SPR-C6A9G	Difficult to measure, > 30	Difficult to measure, > 30	31.8	52.3	Lump shape

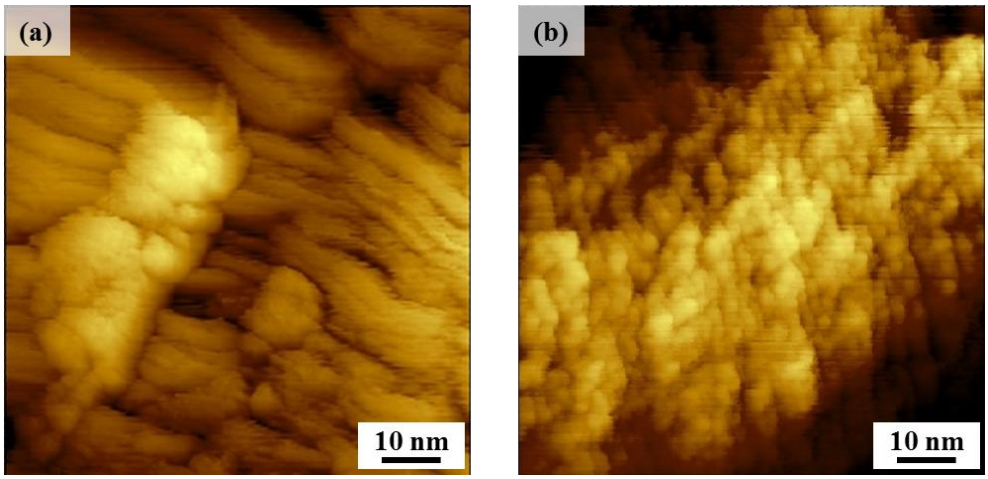

Fig. 4-1. Scanning tunneling microscopy (STM) images of (a) graphitized needle coke and (b) graphitized isotropic coke.

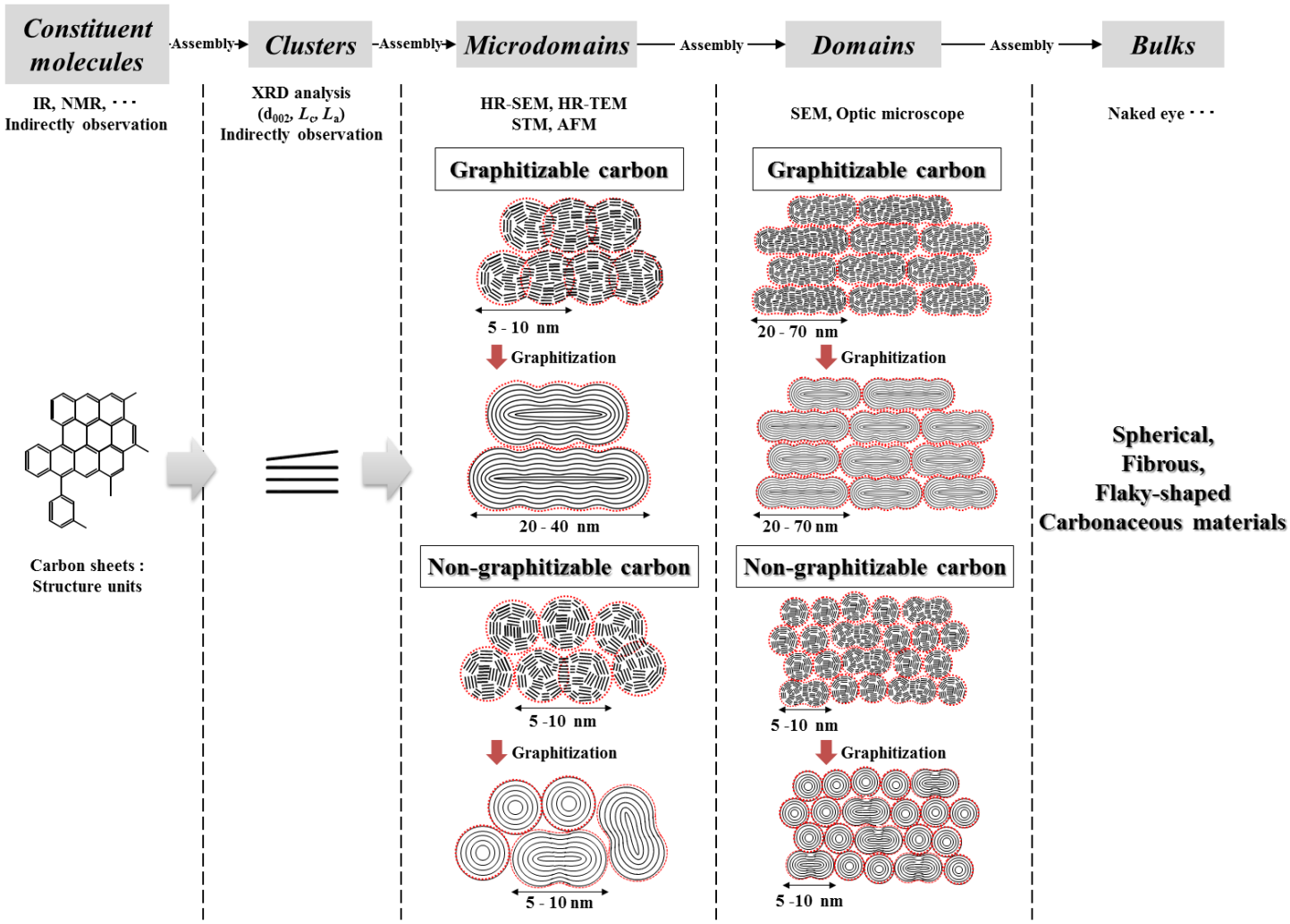

Fig. 4-2. Hierarchical domain structure model of graphitizable carbon (GC) and non graphitizable carbon (NGC).

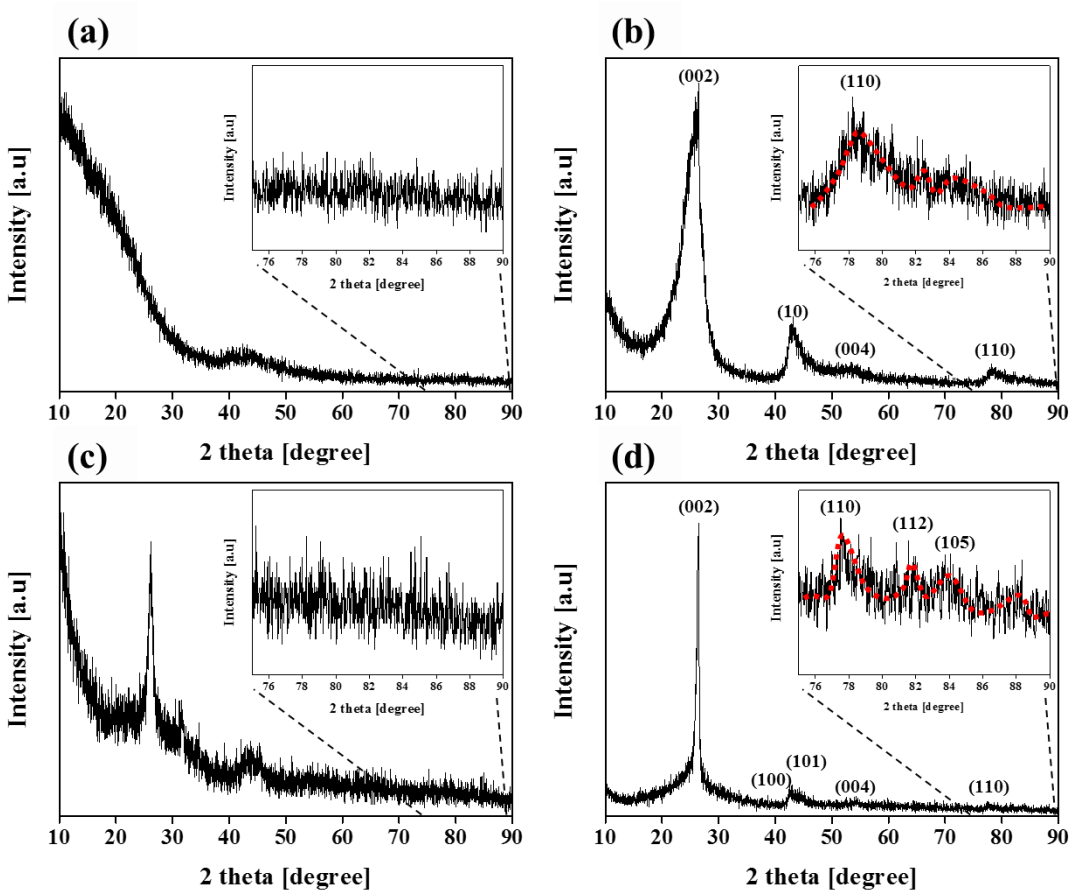

Fig. 4-3. X-ray diffraction (XRD) patterns of (a) SPR-C6, (b) SPR-C6G, (c) SPR-C6A9 and (d) SPR-C6A9G. SPR-C6: pre-heated treated carbon; SPR-C6G: graphitized SPR C6; SPR-C6A9: NaOH-treated SPR-C6; SPR-C6A9G: graphitized SPR-C6A9.

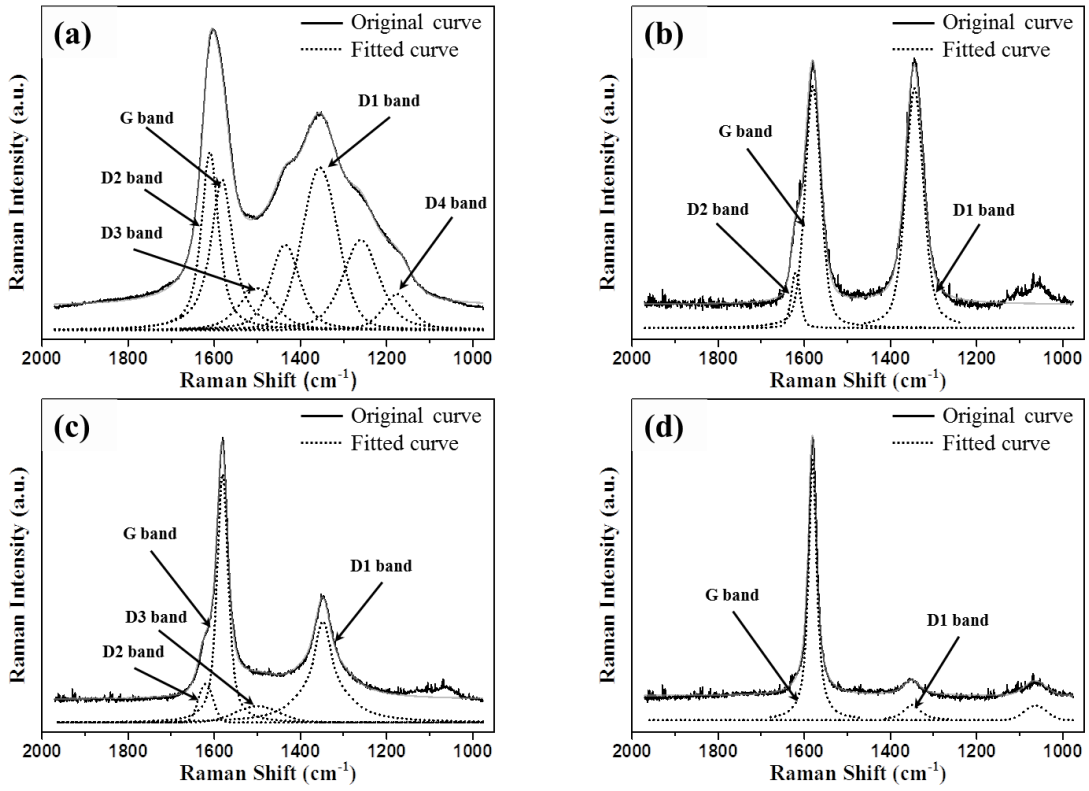

Fig. 4-4. Raman spectra of (a) SPR-C6, (b) SPR-C6G, (c) SPR-C6A9 and (d) SPR-C6A9G.

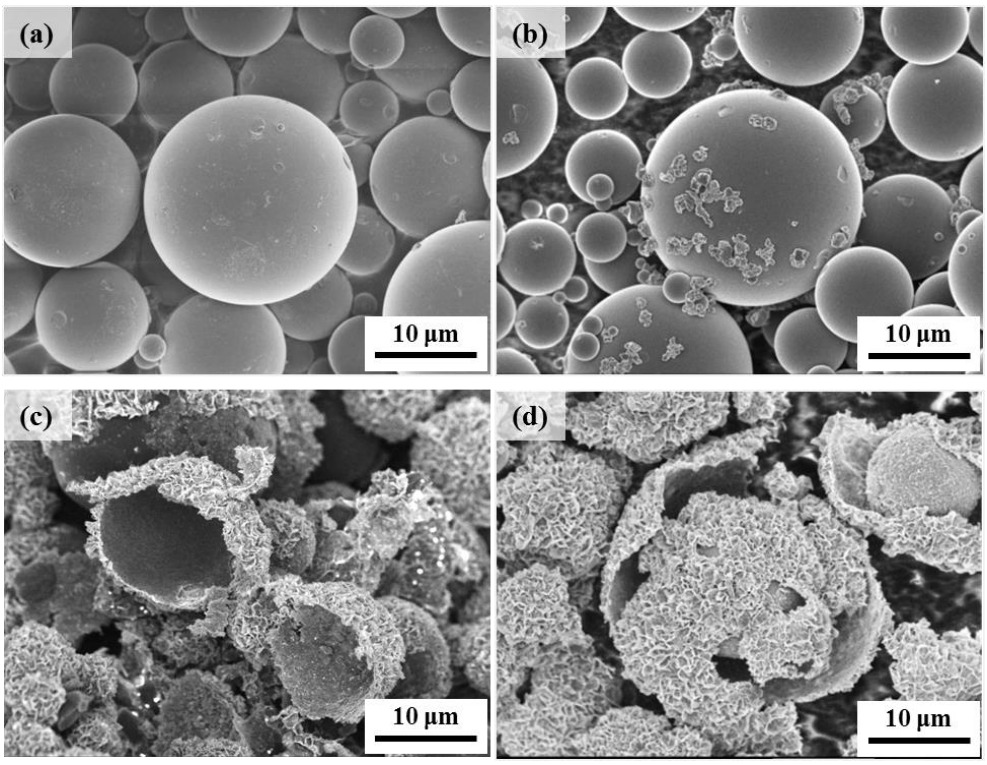

Fig. 4-5. Scanning electron microscopy (SEM) images of (a) SPR-C6, (b) SPR-C6G, (c) SPR-C6A9, and (d) SPR-C6A9G.

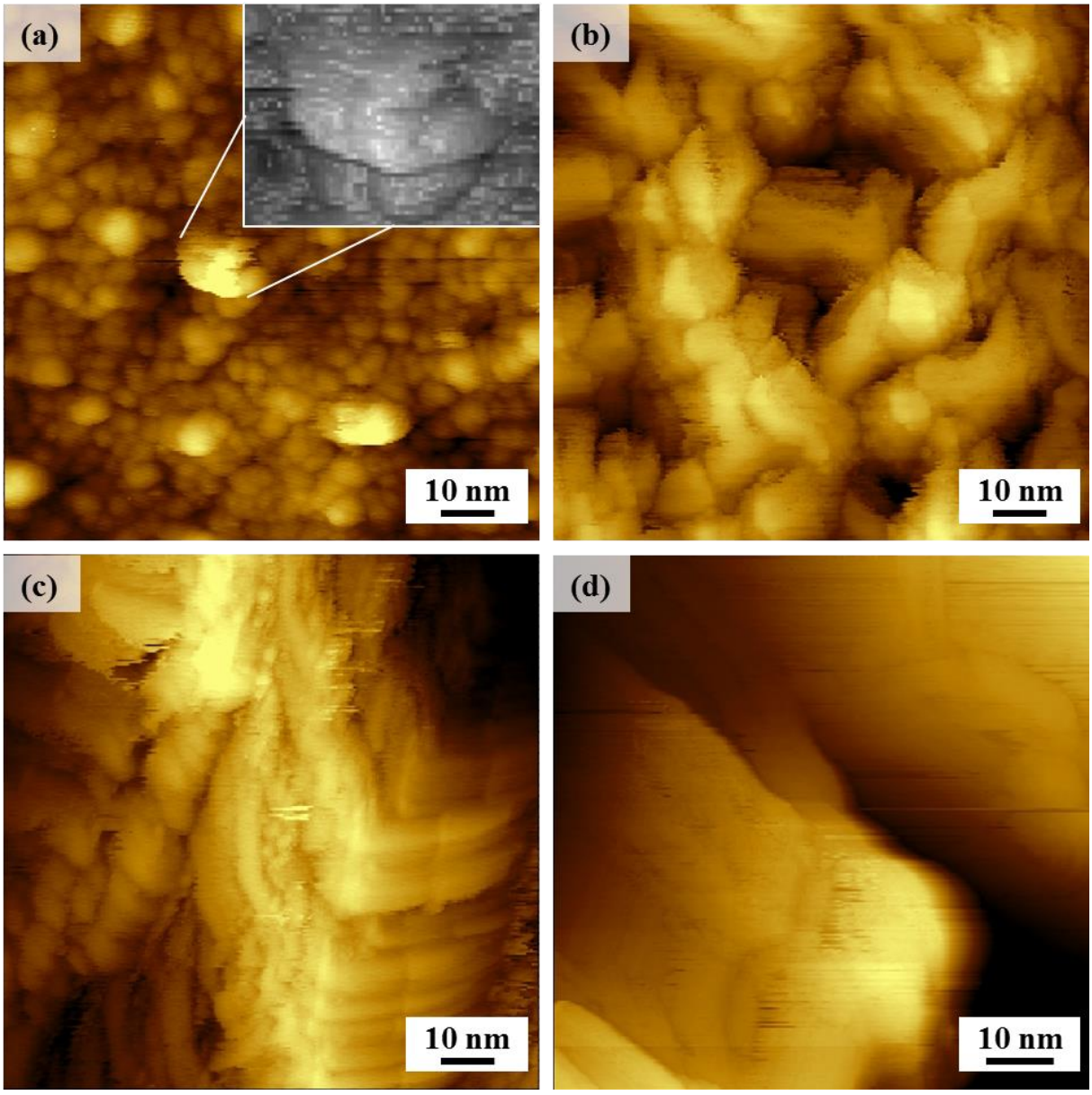

Fig. 4-6. Scanning tunneling microscopy (STM) images of (a) SPR-C6, (b) SPR-C6G, (c) SPR-C6A9 and (d) SPR-C6A9G.

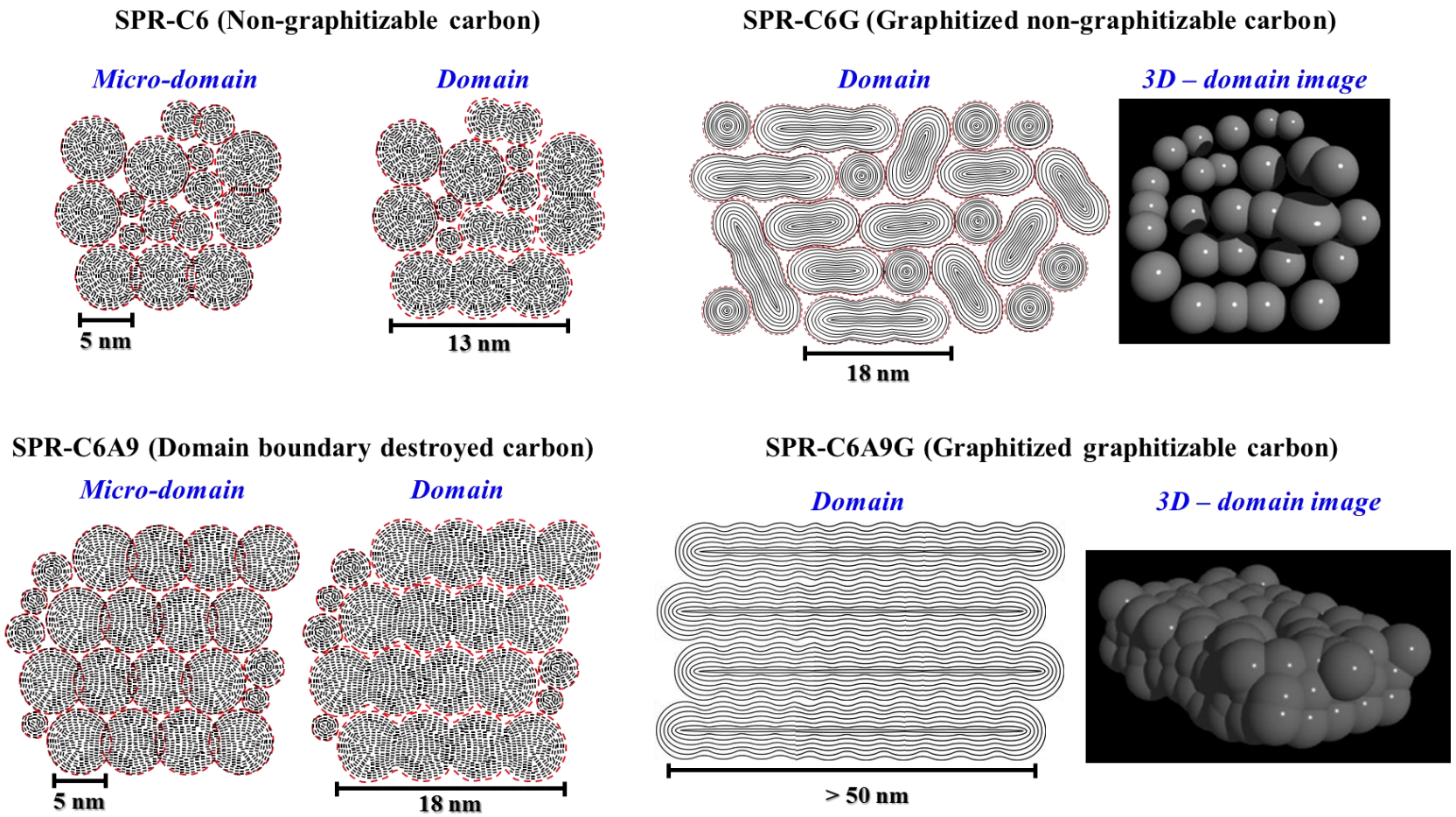

Fig. 4-7. Structural domain model of non-graphitizable carbon (NGC) and graphitizable carbon (GC).

4.4. Conclusions

The preparation of highly graphitized carbon from non-graphitizable raw material was investigated using the hierarchical domain structure model. By NaOH treatment, which plays a role in destroying and reconstructing domain boundaries, we successfully changed NGC to GC by this novel method. The outcomes of this novel method affected the nanostructure, as assessed with XRD and Raman spectroscopy; the meso-structure, as assessed with STM; and the macrostructure, as assessed with SEM. Especially, the microdomains of NGCs showed distinct boundaries and independent structures that hindered or limited the degree of graphitization at the mesoscopic level. However, this limiting structure was changed by destroying the microdomain boundaries, thereby initiating rearrangement. The rearranged structure was similar to that of typical GC, such as needle coke and meso-phase carbon fibers, which are arranged in one direction with an elongated shape. Thus, with this novel method, and the hierarchical structural model, our findings suggest that changing the domain structure can change the properties of the carbon material.

References

[1] Franklin, R. E. "The structure of graphitic carbons." *Acta Crystallographica* **4** (1951): 253–261.

[2] Warren, B. E. "X-ray diffraction in random layer lattices." *Physical Review* **59** (1941): 693.

[3] Inagaki, M., Kang, F. *Carbon Materials Science and Engineering: From Fundamentals to Applications*. Tsinghwa University Press, Beijing, 2006.

[4] Kinney, CR. Studies on producing graphitizable carbons. Proceedings - 2nd Biennial Conference, American Carbon Society. 1955.

[5] Campbell, F. C. *Structural Composite Materials*. ASM International, 2010.

[6] Franklin, R. E. "Crystallite growth in graphitizing and non-graphitizing carbons." *Proceedings of the Royal Society of London A: Mathematical, Physical and Engineering Sciences*. The Royal Society, **209** (1951).

[7] Shiraishi M. *Kaitei Tansozairyou Nyuumon (Japanese)*. (1984): 29–44.

[8] Yoon, S. H., et al. "Axial nano-scale microstructures in graphitized fibers inherited from liquid crystal mesophase pitch." *Carbon* **34** (1996): 83–88.

[9] Mochida, I., et al. "Microstructure of mesophase pitch-based carbon fiber and its control." *Carbon* **34** (1996): 941–956.

[10] Mochida, I., et al. "Progress and effectiveness of structural models of carbons." *Tanso (Japanese)* **215** (2004): 274–284.

[11] Shiratori, N., et al. "Pore structure analysis of activated carbon fiber by microdomain-based model." *Langmuir* **25** (2009): 7631–7637.

[12] Li, W., et al. "Structural features of polyacrylonitrile-based carbon fibers." *Journal of Materials Science* **47** (2012): 919–928.

[13] Ōya, A., et al. "An electron microscopic study on the turbostratic carbon formed in phenolic resin carbon by catalytic action of finely dispersed nickel." *Carbon* **17** (1979): 71–76.

[14] Ōya, A., and Ōtani, S. "Catalytic graphitization of carbons by various metals." *Carbon* **17** (1979): 131–137.

[15] Ōya, A., and Marsh, H. "Phenomena of catalytic graphitization." *Journal of Materials Science* **17** (1982): 309–322.

[16] Inagaki, M, Meyer, R. A. Chemistry and Physics of carbon. (1999): 149–242.

[17] Noda, T., and Kato, H. "Heat treatment of carbon under high pressure." *Carbon* **3** (1965): 289–297.

[18] Inagaki, M., Horii, K., and Naka, S. "Graphitization of carbon beads under pressure." *Carbon* **13** (1975): 97–101.

[19] Hirano, S., Inagaki, M., and Saito, H. "Cooperative accelerating effect of calcium carbonate and gaseous nitrogen on graphitization of carbon." *Carbon* **17** (1979): 395–398.

[20] Noda, M, Inagaki, M, Hirano, S, Saito, H. Accelerating effect of calcium carbonate graphitization of carbon under pressure. *The Journal of the Society of Chemical Industry*, Japan **72** (1969): 643–648.

[21] Yoon, S. H., et al. "KOH activation of carbon nanofibers." *Carbon* **42** (2004): 1723–1729.

[22] Tai F. C, et al. "Raman and X-ray diffraction analysis on unburned carbon powder refined from fly ash." *Journal of Raman Spectroscopy* **41** (2010): 933–937.

[23] Kercher, A. K., Nagle, D. C. "Microstructural evolution during charcoal carbonization by X-ray diffraction analysis." *Carbon* **41** (2003): 15–27.

[24] Sadezky, A., et al. "Raman microspectroscopy of soot and related carbonaceous materials: spectral analysis and structural information." *Carbon* **43** (2005): 1731–1742.

[25] Yoshida, A., Yutaka, K., and Yoshihiro, H. "Full width at half maximum intensity of G band in first order Raman spectrum of carbon material as a parameter for graphitization-a study with pyrolytic carbons." *Tanso (Japanese)* **221** (2006): 2–7.

[26] Lillo-Ródenas, M. A., Cazorla-Amorós, D., and Linares-Solano, A. "Understanding chemical reactions between carbons and NaOH and KOH: an insight into the chemical activation mechanism." *Carbon* **41** (2003): 267–275.

[27] Kim, DW, Kil, HS, Nakabayashi, K, Yoon, SH, Miyawaki, J. "Structural elucidation of physical and chemical activation mechanisms based on the microdomain structure model." *Carbon* **114** (2017): 98–105.

Chapter 5

Improvement of electrical conductivity of non-graphitizable carbon material *via* breaking-down and merging of microdomains

5.1. Introduction

Electrical conductivity is one of the most important physical properties for the effective applications of carbon materials [1]. Such a property has been recognized to be affected by the composed molecules and their orientation of carbon material. Carbon material is commonly classified into graphitizable and non-graphitizable carbons (GC and NGC, respectively), according to the degree of graphitization after heat treatment above 2400°C ("graphitization") [2-4]. At a temperature above 2400°C, the graphitized GC is composed of the large stackings of well-developed oriented hexagonal carbon layers (graphenes), such as single-crystal graphite, which has usually high electrical and thermal conductivities [5,6]. In contrast to GC, NGC is usually difficult to convert to highly graphitized carbon, even after heat treatment above the graphitization temperature because of its randomly oriented small graphene stackings [7-10].

Franklin reported a relationship between the molecular structure of such carbon precursors and their graphitization behaviors, based on XRD analyses of various carbonaceous materials in 1951 [4]. In the Franklin model, GCs show an oriented molecular structure (parallel and regular), whereas the molecular orientation of NGCs is essentially random. Such differences of the graphene stacking and orientation have been considered to be key reasons for the differences of the electrical and thermal conductivities.

In 1996, our group has newly proposed a novel structural model of carbon materials based on microdomain and domain structural units that could restrict the magnitude of graphene molecular crystalline development in the graphitized GCs. For the analysis of mesophase pitch based carbon fiber, we proposed that domains, composed of microdomains (quasi-aligned molecular assembly units), in the mesophase pitch were closely packed, being aligned but incompletely connected; this configuration restricted an increase of the graphitic degree after the graphitization treatment [11]. We also improved the domain-based structural analysis of carbon material into a hierarchical domain structural analysis [12]. The hierarchical domain structural analysis of carbon material can be explained as the serial formation of carbon structures from molecules (e.g., a hexagonal carbon layer), molecular assemblies (e.g., stacked units), microdomains (an assembly of stacked units), domains (an assembly of microdomains), and bulk (an assembly of domains). Based on this hierarchical domain structural analysis, we define a GC as being composed of domains that have partially merged microdomains, whereas a NGC is composed of domains that have few or no merged (almost independent) microdomains. Thus, in a hierarchical domain structural analysis, GCs have larger domain sizes, of 20–70 nm, composed of partially merged microdomains, whereas NGCs have similar or slightly larger domains with microdomains of 5–15 nm. From this hierarchical analysis, we can be sure that the structural conversion of NGC to GC, *that is*, the successful conversion of NGC domain to GC one, enables a preparation of the well-developed graphitic carbon with high electrical conductivity from even the NGC material.

Highly graphitized carbons are applicable to various fields where high electric and thermal conductivities, and high corrosion resistance are required. However, GC precursors, such as mesophase pitch, needle coke, and anisotropic coke having domain structure, are expensive and have poor processability. Thus, if it becomes possible to prepare highly graphitized

carbons from cheap and processable NGC precursors, the application area should be expanded. For example, although it is hard to form a film of mesophase pitch, cheap ones made of polyvinyl chloride (PVC) and chlorinated polyvinyl chloride (CPVC), which are typical NGCs, are easily available. Using such PVC and CPVC films, it would be possible to prepare graphitic thin film with high thermal conductivity, which could be used as a heat release part of IT circuits.

In this study, we have tried the conversion of the domain structure of typical NGC material of carbonized spherical phenol resin into the GC domain structure through the KOH treatment. After the graphitization at 2800℃, the electrical conductivity of the graphitized domain modified sample was evaluated.

5.2. Experimental

5.2.1. Sample preparation

A spherical phenol resin (BEAPS series, Asahi Yukizai Corporation, Japan) carbonized at 600°C for 1 h in a flow of N_2, was used as a starting material (C6). To modify the domain structure, C6 was heat-treated with KOH (purity > 97.0%; Wako Pure Chemical Industries, Ltd., Japan) at 900°C for 1 h using a ramping rate of 5°C min^{-1} in N_2 flow (100 mL min^{-1}). The weight ratio of KOH/C6 was set to 6. After the heat treatment with KOH, the remaining KOH and its decomposed species were washed away with 10% HCl aqueous solution and deionized water until the wash water became at pH ≈ 7. After the washing, the collected sample was dried at 100°C for 3 h in an air oven and dried again at 150°C for 12 h in a vacuum oven. Thus obtained sample was named as C6K9. Then, C6 and C6K9 were further heat-treated at 2800°C for 10 min under an Ar atmosphere, in a horizontal tubular-type graphitization furnace (Kurata Giken Co., Ltd., Japan).

5.2.2. Characterization

To observe changes in the microdomains, STM observation of the prepared samples was carried out after heat treatment at 600°C under a H_2:Ar (1:4) atmosphere, to remove noise originating from heteroatoms. The STM images were acquired in constant current mode (current range: 0.1–1.0 nA; bias voltage: 0.1–2.0 V; scan frequency: 1–2 Hz) using an Agilent Technologies 5500 Scanning Probe Microscope (Toyo Corporation, Japan). Morphology of samples was observed using SEM (JSM-6700F, JEOL, Japan). XRD analyses were performed using a RINT 2200 diffractometer (Rigaku, Japan) with Cu-Kα radiation

(wavelength, λ: 0.15406 nm), generated at 40 kV and 30 mA. Scans were performed at 1.0° min^{-1} for 2θ values between 10° and 90°. Crystallographic parameters (L_c(002), and L_a(110)) were calculated using the Bragg and Scherrer equations [13.14]. Raman spectra were obtained with a Raman spectrometer (NRS-3000, JASCO, Japan) using a 532-nm Ar-ion laser as the excitation source. The first-order Raman spectra of samples were deconvoluted using four disordered (D1, D2, D3, and D4) bands and one ordered (G) band combination [15].

Electrical resistance, *R*, was measured for sheet type samples by using a digital multimeter (CMD-2000d, Custom. Taiwan). To prepare the sheet type sample, a mixture of the prepared carbon material (95 wt.%) and polytetrafluoroethylene as a binder (5 wt.%) was pressed at 15 MPa. Specific electrical resistance, ρ, was calculated by an equation of $\rho=RA/t$, where *A* and *t* are area and thickness of the sample, respectively.

5.3. Results and discussion

Table 5-1 shows changes of specific electrical resistances, ρ, of C6 and C6K9, and their graphitized samples (C6-H2800 and C6K9-H2800, respectively). C6 of non-graphitizable characteristics showed relatively high ρ value of 115.2 Ω cm. After the graphitization at 2800°C, it decreased to 21.9 Ω cm due to the arrangement of a part of the structure by the high temperature treatment. On the other hand, KOH-treated sample (C6K9) showed specific electrical resistance of 46.3 Ω cm, which was much lower than the starting material (C6). After the heat-treatment at 2800°C, C6K9-H2800 showed much less than half ρ value of C6-H2800 (8.5 Ω cm), suggesting that non-graphitizable structure of C6 was changed into graphitizable one by the KOH treatment.

In Fig. 1, micrometer-scale morphological images of C6 and C6K9 together with their graphitized samples obtained using SEM are shown. Spherical shape with smooth surfaces of C6 was observed. Graphitization of C6 did not induce detectable changes in shape and size (C6-H2800). In case of the KOH-treated sample (C6K9), on the other hand, the surface became somewhat rough with maintaining the original spherical shape. After the graphitization, the morphology remained unchanged (C6K9-H2800 vs. C6K9).

Since the micrometer-scale morphology was almost unchanged by the KOH treatment except for the surface roughness as found in Fig. 5-1, the transformation from non-graphitizable to graphitizable would be induced by a change of nanometer-scale structures. To investigate nanometer-scale morphology, such as microdomain and domain structures, STM was applied. As shown in Fig. 5-2, C6 showed independent spherical microdomains of 2–5 nm in diameter. After the graphitization, C6-H2800 showed slightly larger domains (5–18 nm) because a part of microdomains was co-shared with others. The observed

microdomain and domain structures of C6 and C6-H2800 were typical for non-graphitizable carbons. Contact resistance at boundaries of independent microdomains and domains was considered to interfere the movement of electrons, giving rise to high ρ values. C6K9, the KOH-treated sample, did not show significant changes in size and shape of microdomains as reported previously [16]. After the 2800°C-heat-treatment, however, the coalescence of microdomains became more apparent: Large numbers of microdomains were merged with each other to form large domains. In addition, the boundaries between the domains become more blurred. In Table 5-1, microdomain and domain sizes estimated from the STM observation were also summarized.

To increase the electrical conductivity of carbon materials, degree of graphitization and quantity and type of defects are important factors, which can be estimated from XRD and Raman spectroscopy results, respectively. Fig. 5-3 shows XRD profiles of C6, C6K9, and their graphitized samples. C6 showed very obscure peaks of (002), (10), and (110) diffractions, indicating the undeveloped carbon structure. After graphitization 2800°C, much clearer peaks were observed, whilst the peak broadness indicated the low degree of graphitization (C6-H2800). After the KOH-treatment of C6, on the other hand, a broad peak at 2θ = 15–30° was disappeared. By the heat-treatment at 2800°C, C6K9-H2800 showed well-developed and distinct peaks, indicating an increase of the graphitization degree. L_c(002) and L_a(110) values of C6-H2800 and C6K9-H2800 were well-matched with domain size (Table 5-1). This suggests that the graphitic structure was developed the whole length of each domain. In other words, size of domains (a nanometer-scale character) of carbon material governed the electronic conductivity (a macroscopic property).

Fig. 5-4 showed Raman spectra of C6, C6K9, C6-H2800, and C6K9-H2800. Peaks at ~1200 (D4), ~1500 (D3), and ~1620 cm^{-1} (D2) were attributed to sp^3 carbon or impurities,

amorphous carbon, and disordered carbon, respectively [15]. The strong D1 (disorder) band at ~1350 cm^{-1} and many disordered peaks of C6, typical characteristics of non-graphitizable carbon, persisted even after the graphitization at 2800°C (C6-H2800). In the case of C6K9, similar peaks with C6 were observed. For C6K9-H280, however, most of disorder bands were remarkably weakened or disappeared. Relative intensities of the D band to that of the G band, I_D/I_G, and full-width at half-maximum of G band (G-FWHM) [17], which can be used as indices of the degree of graphitization, are also tabulated in Table 5-1. Low I_D/I_G ratio of 0.46 again indicated that non-graphitizable feature of C6 was turned into a graphitizable one by the KOH treatment. In addition, C6K9-H2800 showed G-FWHM value of 27.4 cm^{-1} which was much lower than C6-H2800 (43.2 cm^{-1}). From XRD and Raman spectroscopic results, it was confirmed that the non-graphitizable C6 was converted graphitizable carbon by the KOH treatment, giving rise to the remarkable lowering of electrical resistance of C6K9-H28

Table 5-1. Specific electrical resistance (ρ), sizes of microdomain and domain, X-ray diffraction crystalline parameters (L_c(002) and L_a(110)), relative intensities of D band to that of G band (I_D/I_G), and full width at half maximum intensity of G band (G-FWHM) in the first-order Raman spectra of C6, C6K9, and their heat-treated samples (C6-H2800 and C6K9-H2800, respectively).

Sample	Specific electric resistance, ρ [Ω cm]	STM		XRD		Raman	
		Microdomain size [nm]	Domain size [nm]	L_c(002) [nm]	L_a(110) [nm]	I_D/I_G [-]	G-FWHM [cm^{-1}]
C6	115.2	2–5	2–13	Not measurable	Not measurable	1.09	61.7
C6K9	46.3	2–5	2–13	Not measurable	Not measurable	1.04	112.0
C6-H2800	21.9	2–10	5–18	4.7	16.9	0.99	43.2
C6K9-H2800	8.5	> 25 nm	> 25 nm	20.3	22.7	0.46	27.4

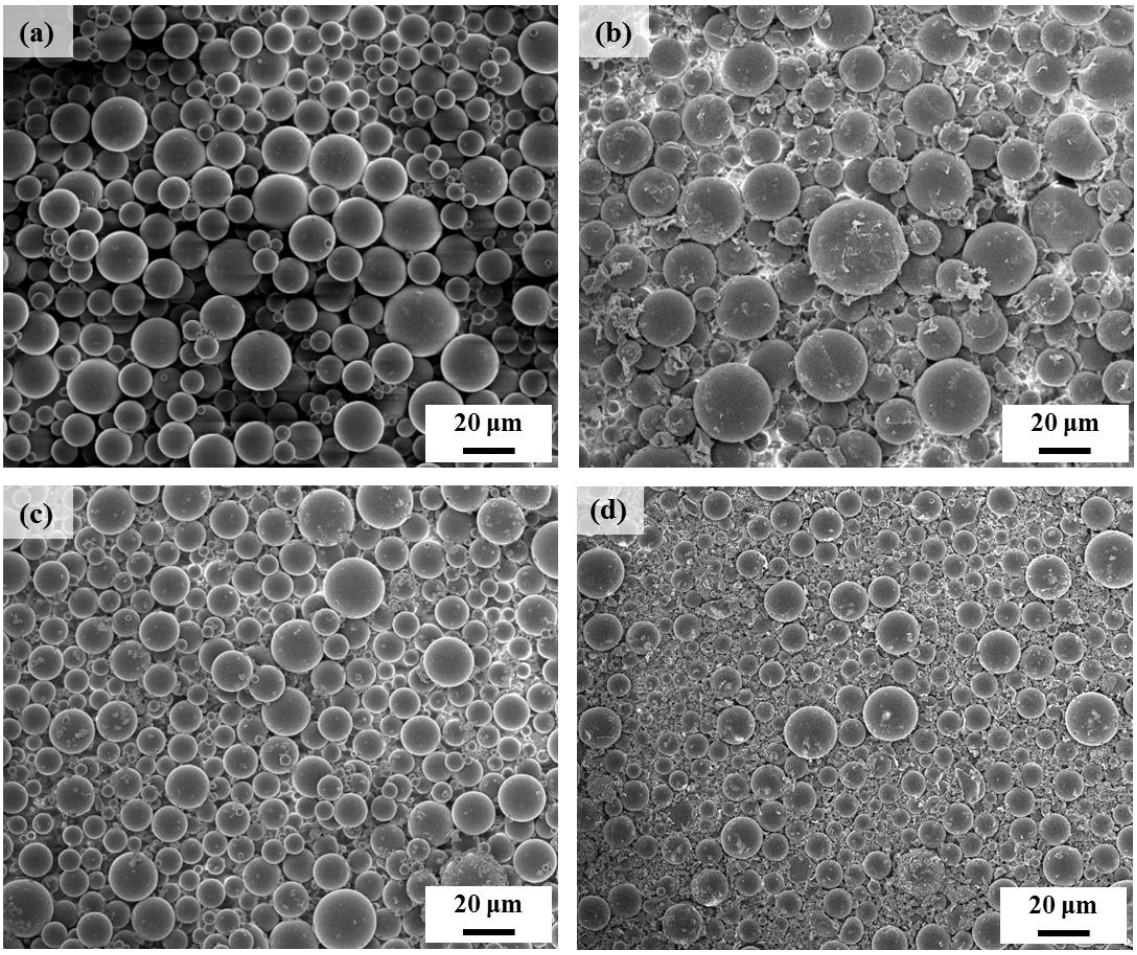

Fig. 5-1. Scanning electron microscopy (SEM) images of (a) C6, (b) C6K9, (c) C6-H2800, and (d) C6K9-H2800.

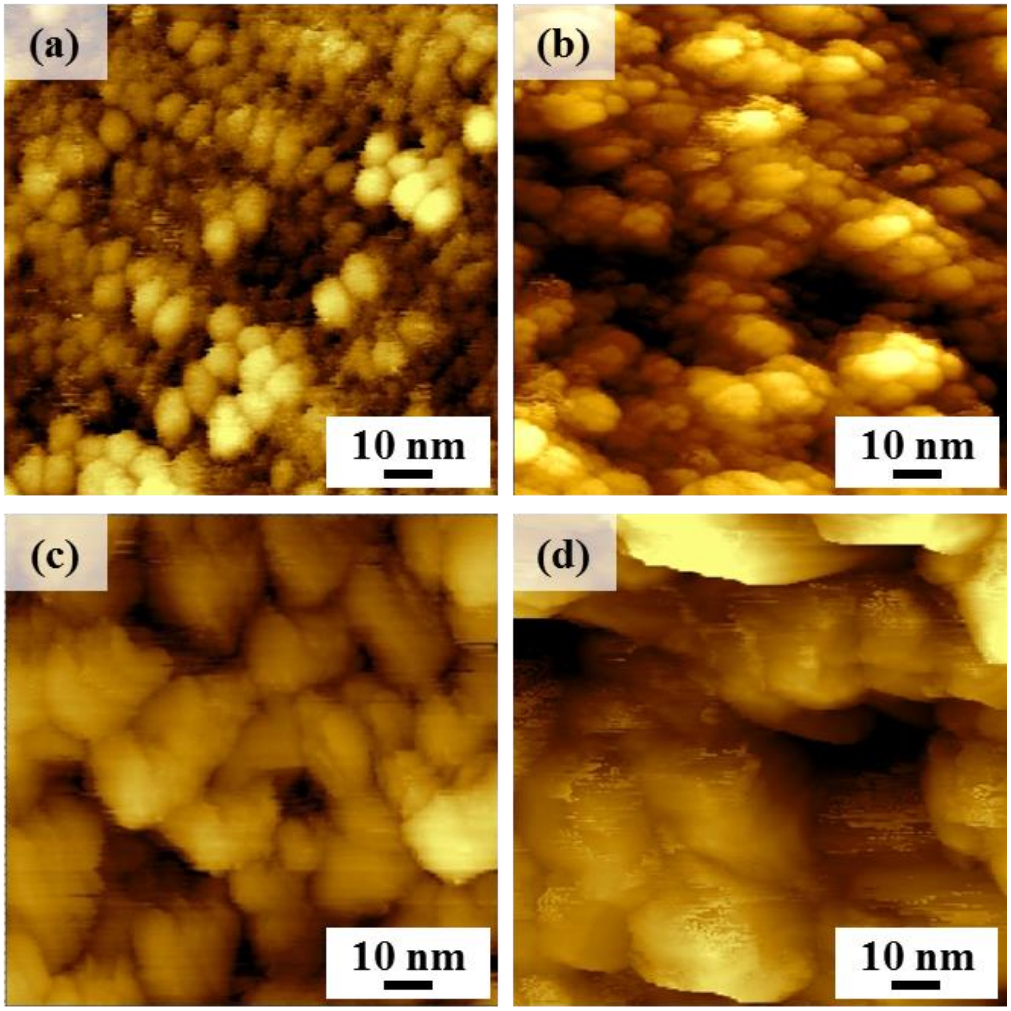

Fig. 5-2. Scanning tunneling microscopy (STM) images of (a) C6, (b) C6K9, (c) C6-H2800, and (d) C6K9-H2800.

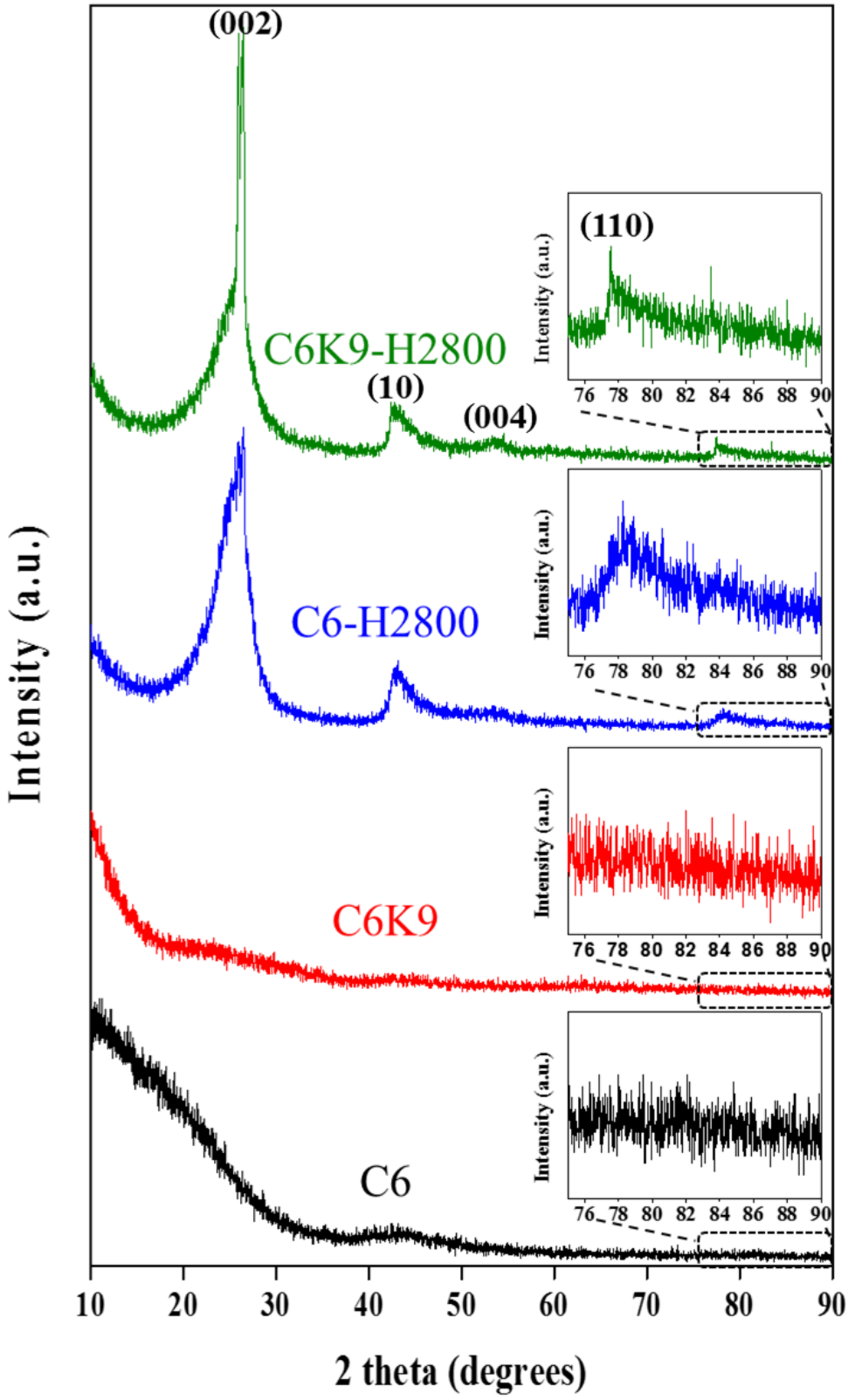

Fig. 5-3. X-ray diffraction (XRD) patterns of C6, C6K9, C6-H2800 and C6K9-H2800.

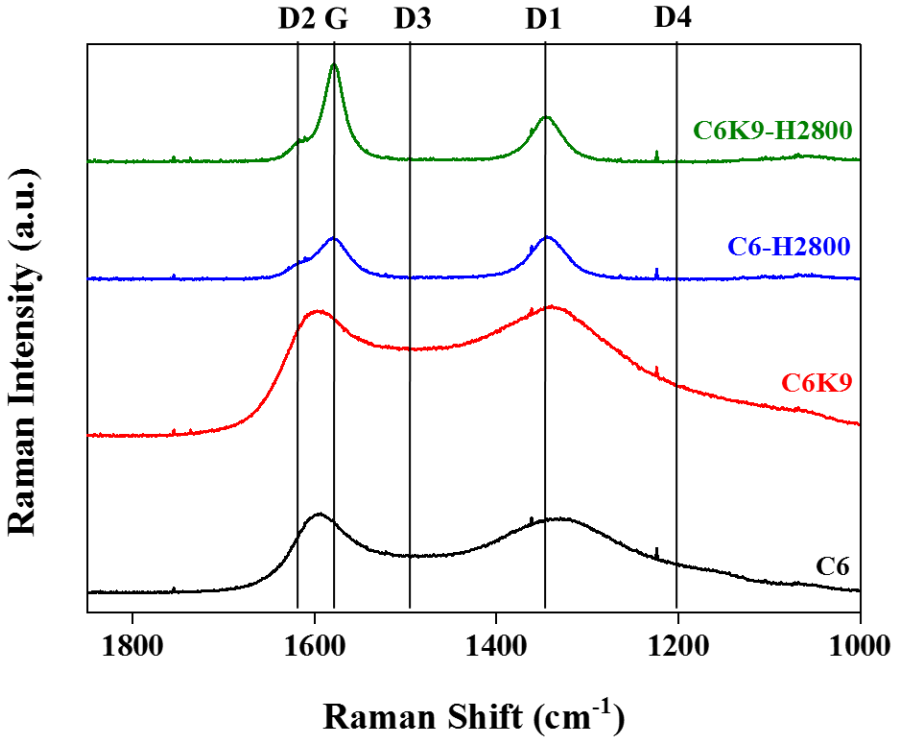

Fig. 5-4. Raman spectra of C6, C6K9, C6-H2800 and C6K9-H2800.

5.5. Conclusions

Graphitizable carbon was prepared via breaking-down and merging of boundaries of microdomains from non-graphitizable carbon using potassium hydroxide (KOH). The structural changes of microdomains and domains in prepared graphitizable carbon were confirmed using XRD, Raman spectroscopy, and STM. In addition, after the graphitization at 2800℃, graphitized KOH-treated sample showed much less than half (about 39%) electric resistance value of graphitized non-graphitizable carbon, suggesting that non-graphitizable structure was changed into graphitizable one by the KOH treatment. From this results, we concluded that control of the nanometer-scale structure of microdomains and domains is one of the key issues to control the macroscopic properties of the carbon material.

References

[1] Chung, D. D. L. "Electrical applications of carbon materials. "*Journal of Materials Science* **39** (2004): 2645–2661.

[2] Inagaki, M., and Kang, F. *Carbon Materials Science and Engineering: From Fundamentals to Applications*. Tsinghwa University Press, Beijing, (2006).

[3] Franklin, R. E. "The structure of graphitic carbons." *Acta Crystallographica* **4** (1951): 253–261.

[4] Franklin, R. E. "Crystallite growth in graphitizing and non-graphitizing carbons." *Proceedings of the Royal Society of London A: Mathematical, Physical and Engineering Sciences*. The Royal Society, **209** (1951).

[5] Bernal, J. D. "The structure of graphite." *Proceedings of the Royal Society of London. Series A, Containing Papers of a Mathematical and Physical Character* **106** (1924): 749–773.

[6] Hassel, O., and Mark, H. "Über die Kristallstruktur des Graphits." *Zeitschrift für Physik* **25** (1924): 317–337.

[7] Lipson, H., and Stokes, A. R. "A new structure of carbon." *Nature* **149** (1942): 328–328.

[8] Lipson, H., and Stokes, A. R. "The structure of graphite." *Proceedings of the Royal Society of London A: Mathematical, Physical and Engineering Sciences*. The Royal Society, **181** (1942).

[9] Warren, B. E. "X-Ray Diffraction Study of Carbon Black." *The Journal of Chemical Physics* **2** (1934): 551–555.

[10] Bacon, G. E. "Unit-cell dimensions of graphite." *Acta Crystallographica* **3** (1950): 137–139.

[11] Yoon, S. H., et al. "Axial nano-scale microstructures in graphitized fibers inherited from liquid crystal mesophase pitch." *Carbon* **34** (1996): 83–88.

[12] Mochida, I., et al. "Progress and effectiveness of structural models of carbons." *Tanso* **215** (2004): 274–284.

[13] Tai, F. C., et al. "Raman and X-ray diffraction analysis on unburned carbon powder refined from fly ash." *Journal of Raman Spectroscopy* **41** (2010): 933–937.

[14] Kercher, Andrew K., and Dennis C. Nagle. "Microstructural evolution during charcoal carbonization by X-ray diffraction analysis." *Carbon* **41** (2003): 15–27.

[15] Sadezky, A., et al. "Raman microspectroscopy of soot and related carbonaceous materials: spectral analysis and structural information." *Carbon* **43** (2005): 1731–1742.

[16] Kim, DW, Kil, HS, Nakabayashi, K, Yoon, SH, Miyawaki, J. "Structural elucidation of physical and chemical activation mechanisms based on the microdomain structure model." *Carbon* **114** (2017): 98–105.

[17] Yoshida, A., Kaburagi, Y., and Hishiyama. Y. "Full width at half maximum intensity of G band in first order Raman spectrum of carbon material as a parameter for graphitization-a study with pyrolytic carbons." *Tanso (Japanese)* **221** (2006): 2–7.

Chapter 6

General conclusions

Based on the hierarchical domain structural model, structural and functional controls of carbon materials were performed. Using the microdomain which is the basic structural unit of all artificial carbon materials, structure analysis of pore development process (activation mechanism) by prepared different methods of activated carbons, and control of properties (graphitization degree and electrical resistance) were well elucidated.

The conclusions related to the structure analysis and function control of carbon materials in the respective chapters are summarized as follows;

Chapter 2. Observation of domain structure in various carbon materials

From the observation of existence of domain structure in various artificial carbon materials, it revealed that microdomain is basic structural unit for all artificial carbon materials.

Domain structures in various artificial carbon materials were observed using the scanning tunneling microscopy (STM), and revealed that microdomain are basic structural unit for all artificial carbon materials. In addition, the difference of the size and shape of microdomains depending on the precursors and preparation method was confirmed. Therefore, considering of the previous domain studies, the domain structure will affect the structural and functional controls of the artificial carbon materials.

Chapter 3. Structural elucidation of physical and chemical activation mechanisms based on the microdomain structure model

Based on the microdomain structure model, the difference in the pore development mechanisms between physical (Steam) and Chemical (KOH) activation were clearly explained.

The different structural mechanisms of KOH and steam activations for AC preparation were explained based on the microdomain structure model. In the steam activation process, the sizes of both the microdomains and the particles decreased by inhomogeneous gasification; micropores formed only for a portion of the remaining microdomains. Thus, steam activation gave the lower yield and limited porosity. In contrast, KOH activation provided uniform pore development overall for microdomains consisting of carbon particles; the higher yield and superior pore development were attributed to the catalytic role of the potassium species produced during activation. The proposed structural mechanism model for pore development with physical and chemical activations is expected to serve as a guideline for developing ACs with highly controlled pore structures.

Chapter 4. Highly graphitized carbon from non-graphitizable raw materials and its formation mechanism based on the domain theory

The finding of a novel method to convert non-graphitizable carbon into graphitizable carbon, and to analyze the conversion mechanism were performed based on the hierarchical domain structural model.

The preparation of highly graphitized carbon from non-graphitizable raw material was investigated using the hierarchical domain structure model. By NaOH treatment, which plays a role in destroying and reconstructing domain boundaries, NGC to GC by this novel method was successfully changed. The outcomes of this novel method affected the nanostructure, as assessed with XRD and Raman spectroscopy; the meso-structure, as assessed with STM; and the macrostructure, as assessed with SEM. Especially, the microdomains of NGCs showed

distinct boundaries and independent structures that hindered or limited the degree of graphitization at the mesoscopic level. However, this limiting structure was changed by destroying the microdomain boundaries, thereby initiating rearrangement. The rearranged structure was similar to that of typical GC, such as needle coke and meso-phase carbon fibers, which are arranged in one direction with an elongated shape. Thus, with this novel method, and the hierarchical structural model, our findings suggest that changing the domain structure can change the properties of the carbon material.

Chapter 5. Improvement of electrical conductivity of non-graphitizable carbon material via breaking-down and merging of microdomains

Based on the domain structure, relationships between the graphitized domain modified carbon (structure) and electrical conductivity (macroscopic function) were evaluated.

Graphitizable carbon (GC) was prepared via breaking-down of boundaries of microdomains from non-graphitizable carbon (NGC) using potassium hydroxide (KOH). The structural changes of microdomains and domains in prepared GC were confirmed using XRD, Raman spectroscopy, and STM. In addition, after the graphitization at 2800℃, graphitized KOH-treated sample showed less than half electrical resistance value of graphitized NGC, indicating that non-graphitizable structure was successfully changed into graphitizable one by the KOH treatment. The findings in this study pointed out an importance of controlling the nanometer-scale microdomain and domain structures of carbon materials, to improve macroscopic properties, such as electrical conductivity.

As a concluding remark, I revealed that the hierarchical domain structure model can explain close relationships between properties and domain structure of artificial carbon

materials. Although various carbon materials have many future challenges, the hierarchical domain structure model will play an important role to structure analysis, and control of function in carbon materials. I believe that hierarchical domain structure model can be apply the more effectively approaching in artificial carbon materials.

論 文 内 容 の 要 旨

現代社会において炭素材料は、電極材、吸着材、建築物および車体の複合材など多くの分野で使用される非常に重要な材料の一つである。原料（石炭、石油、ポリマー、バイオマスなど）に対して適した処理を施すことにより、高強度や高弾性率炭素繊維、高比表面積の多孔質材、高電気伝導度・高熱伝導度炭素材など、性質が異なるさまざまな材料を製造することができる。炭素材料を形成する炭素六角網面積層の配列が機能物性を支配することは良く認識されているが、より一層の高機能化のためには、炭素材料の正確かつ体系的な構造把握が不可欠である。そこで炭素材料の構造を説明するモデルとして、ドメイン構造モデルが新たに提案された。この構造モデルでは、分子レベルから目に見えるオーダーまでの間をつなぐ構造単位として、グラフェンクラスター、マイクロドメインおよびドメインと呼ばれる中間構造体が提案されている。低次元の構造はより高次元の構造に大きく関係し、ひいては材料の機能物性に大きな影響を与えると考えられる。これまでの研究において、一部の炭素材料においてドメインの存在が確認されているものの、ドメイン構造の変化による物性への影響についての検討は未だ不十分である。

本研究では、炭素材料の高機能化を目的とし、ドメイン構造モデルに基づいた人造炭素材料の構造および機能制御の研究に関する以下の研究を行った。（1）多様な炭素材料のドメイン構造の把握、（2）マイクロドメイン構造モデルに基づく活性炭の賦活メカニズムの解明、（3）マイクロドメイン構造単位の部分的破壊による黒鉛化特性の制御、（4）ドメインの構造制御によるマクロ物性（電気抵抗度）の向上、に関する研究を行った。本研究における知見は、以下のように纏められる。

第1章では、炭素の構造、構造による炭素材料の分類、現在までの炭素材料の構造モデルについて述べた。

第2章では、多様な人造炭素材料について走査径トンネル顕微鏡（STM）を用いて構造観察を行い、マイクロドメインが全ての人造炭素材料について存在する基本構造単位であることを明らかにした。また、原料や調製法により、ドメインのサイズや形状が異なることを見出した。

第3章では、マイクロドメイン構造モデルに基づいて、活性炭の重要な製造工程である賦活のメカニズム解明を行った。物理賦活（水蒸気賦活）と化学賦活（水酸化カリウム（KOH）賦活）により調製した活性炭の粒子およびマイクロドメインの形状およびサイズを走査型電子顕微鏡（SEM）と STM を用いて観察したところ、物理賦活活性炭は高賦活度となるにつれて粒子およびマイクロドメインのサイズが小さくなるのに対して、化学賦活活性炭はいずれのサイズもほぼ一定であることを見出した。一方、化学賦活活性炭は同じ収率において物理賦活活性炭よりも高い細孔発達度を示すことから、物理賦活では炭素粒子とマイクロドメインの不均一なガス化反応により一部のマイクロドメインのみに細孔が発達するのに対し、化学賦活ではカリウム化合物が触媒として働き、炭素粒子を構成する全てのマイクロドメイン全体に亘って均一に細孔が発達すると結論付けた。

第4章では、難黒鉛化性炭素として知られるフェノール樹脂由来炭素材料に対し、マイクロドメイン構造単位を部分的に破壊することで、黒鉛化度の向上を試みた。独立したマイクロドメインとドメイン構造がほぼ同じで存在することであるフェノール樹脂由来炭素材料をそのまま 2800℃熱処理（黒鉛化処理）を施すと、各ドメインは明瞭な境界を持つ独立した構造を示す。これに対し、フェノール樹脂由来炭素材料に対して水酸化ナトリウム（NaOH）を用いて 900℃で1時間処理を施しマイクロドメインの境界を破壊することで、黒鉛化処理時にドメイン構造が再配列し、境界が不鮮明な大きなドメインが形成されることを明らかにした。また、X 線回折、Raman 分光分析の結果、NaOH 処理によるマイクロドメインの境界破壊により、黒鉛化度が顕著に上昇することを見出した。つまり、ドメイン構造単位が黒鉛化特性制御のカギであることを明らかにし、難黒鉛化性炭素においてもマイクロドメイン境界を破壊することで高黒鉛化度を誘導できることを示した。

第5章では、部分的にマイクロドメイン構造単位を破壊した難黒鉛化性炭素に対して 2800℃で熱処理を行い、マイクロドメインの融合度とマクロ物性の一つである電気抵抗度の相関性を調べた。KOH 賦活により構造破壊したフェノール樹脂由来炭素材料を 2800℃で黒鉛化処理を行うと、マイクロドメイン同士が徐々に融合した大きなドメインを形成することを見出した。一方、マイクロドメインの破壊なしの場合、マイクロドメインは個々が独立または少数が融合した形成の小さなドメイン構造を示した。電気抵抗度は、マイクロドメイン境界の破壊がない場合は、黒鉛化処理しても 高い値であったのに対し、構造破壊した難黒鉛化性

炭素においては黒鉛化処理し、非常に低い値を示した。つまり、ドメインというミクロ構造を制御することで電気抵抗度というマクロ物性を向上できることを明らかにした。

第6章では、 本研究で得られた主な成果について総括した。

Acknowledgement

It is my honor and desire to express deep gratitude to Prof. Jin Miyawaki, Prof. Seong-Ho Yoon, and Prof. Koji Nakabayasi for their profound teachings and lessons throughout the past 3 years of my doctoral course which was not only simply hard but also took a lot of endurance and guidance to get on the track and do the job. If it has not been for your help, I hardly think I would have the pleasure of writing this acknowledgement. And, I'd like to express my appreciation to Prof. Hisahiro Einaga for his guidance and help as external readers in spite of their busy schedule.

I acknowledge financial support provided by the JASSO scholarship.

I'd like to express my thanks to group members in Yoon & Miyawaki laboratory for their help, cooperation during my campus life, particularly, Yang Jianxiao, Koichiro Hata, Jinchang Liu, Yao Yu, Chinami Morishima, Yuki Azuma, Motoi Ikeda, Shoki Tanaka, Yusi Fukutani, Toru Kotegawa, Hironori Watanabe, Hiroki shimanoe, Takuya Ito, Syo Yoshida, Kazuki Ito, Yuki Shimobayashi. I also can't forget the kindness of Ms. Keiko Ideta.

I'm deeply grateful to Korean fellows in Chikushi campus, particularly Dr. Hyun-Sig Kil, Dr. Byung-Jun Kim, Dr. Yu-Jin Han, Dr. Jandee Kim, Dongyeon Ryu, Dabin Chung, Hyeon-Seok Yi, Minki Sung. I have enjoyed my campus life with their kind endurance and assistance.

I also want to appreciate Prof. Kap-Seung Yang, who was my supervisor for master's degree. You always encourage and support me. Thank you very much.

Most of all, I'd like to give my special thanks to my parents (Yoon-Jae Kim and Soo-Hee Shin) and sister (Mi-Jin Kim, Mi-Sun Kim). Their endless support and great love made me strong and confident.

Thank you so much.

February, 2017

Doo-Won Kim